

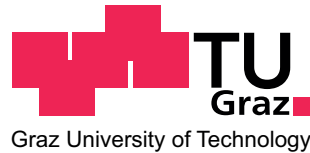
Maximilian Lasserus, BSc

Bimetallic Clusters in Helium Droplets: From the Synthesis to Nanoscale Alloying

Master Thesis

For obtaining the academic degree
Diplomingenieur

Master Programme of Technical Sciences
Technical Physics



Graz University of Technology

Supervisor:

Univ.-Prof. Mag. Dr.rer.nat Wolfgang E. Ernst
Institute of Experimental Physics

Graz, May 2017

Deutsche Fassung:
Beschluss der Curricula-Kommission für Bachelor-, Master- und Diplomstudien vom 10.11.2008
Genehmigung des Senates am 1.12.2008

EIDESSTÄTTLICHE ERKLÄRUNG

Ich erkläre an Eides statt, dass ich die vorliegende Arbeit selbstständig verfasst, andere als die angegebenen Quellen/Hilfsmittel nicht benutzt, und die den benutzten Quellen wörtlich und inhaltlich entnommenen Stellen als solche kenntlich gemacht habe.

Graz, am

.....
(Unterschrift)

Englische Fassung:

STATUTORY DECLARATION

I declare that I have authored this thesis independently, that I have not used other than the declared sources / resources, and that I have explicitly marked all material which has been quoted either literally or by content from the used sources.

.....
date

.....
(signature)

Abstract

Using superfluid helium nanodroplets for the synthesis of clusters and nanowires is a novel but already well-established method. The ultra-cold environment of the droplet provides a unique and nearly perturbation free matrix.

In this thesis, Time of Flight mass spectroscopy was used to analyse monometallic clusters with sizes ≤ 15 atoms. Even-odd oscillation, as well as closed electron shell effects, were observed. Additionally, Time of Flight spectra were used to analyse bimetallic clusters synthesised in helium droplets. Furthermore, their mixing behaviour was observed. A simulation-based investigation indicated a mixing of both components, resulting in a decrease of the pure element signal.

The nanoparticles were deposited onto a heatable carbon grid to be analysed with a transmission electron microscope. Images of different types of core-shell structures were gathered. The heatable carbon grid enables an observation of a temperature depended diffusion process within the core-shell structures. Due to an analysis of the high angle annular dark field (HAADF) images, it was possible to solve the diffusion equation for every temperature to fit the temperature dependent diffusion length.

Kurzfassung

Die Verwendung von Heliumtröpfchen für die Synthese von Cluster und Nanowires ist eine neue, jedoch mittlerweile etablierte Methode. Die sehr kalte Temperatur des Tröpfchens bietet eine einzigartige und fast störungsfreie Umgebung.

In dieser Arbeit wurde Flugzeitmassenspektroskopie verwendet, um metallische Cluster mit Größen ≤ 15 Atomen zu untersuchen. Even-odd Oszillationen in der Größenverteilung wurden genauso wie geschlossene Elektronenschaleneffekte beobachtet. Zusätzlich wurde Flugzeitmassenspektroskopie eingesetzt, um bimetallische Cluster, welche in Heliumtropfen synthetisiert wurden, zu untersuchen. Außerdem wurde das Mischverhalten untersucht. Eine computerunterstützte Auswertung führte zu der Schlussfolgerung, dass sich beide Elemente mischten, was zu einer Abschwächung des Signals des Reinformmetalls führte.

Die Nanoteilchen wurden auf heizbare Kohlenstoffgitter deponiert, um sie unter einem Transmissions Elektronen Mikroskop zu untersuchen. Während der Untersuchung wurden Aufnahmen von verschiedenen Arten von Strukturen gemacht. Das heizbare Gitter ermöglichte es, die temperaturabhängige Diffusion in einem core-shell Teilchen zu beobachten. Durch das Untersuchen von HAADF Aufnahmen war es möglich, die Diffusionsgleichung für jede Temperatur zu lösen und dadurch einen Fit für die temperaturabhängigkeit der Diffusionslänge zu erhalten.

Contents

1	Introduction	1
2	Theoretical Introduction	2
2.1	Helium	2
2.2	Helium Droplets Formation	2
2.3	Pickup of Foreign Atoms	4
2.4	Time of Flight Measurements of Nano Structures	5
2.4.1	Electron Impact Ionisation	5
2.5	Characteristics of Cluster	6
2.5.1	Crystal Structure of a Cluster	6
2.5.2	Deposition on Substrate	7
2.6	Alloys	8
3	Experimental Setup	10
3.1	Source chamber	11
3.1.1	Coldhead	11
3.1.2	Vacuum system	12
3.2	Pickup Chamber	12
3.2.1	Evaporation cells	12
3.2.2	Vacuum system	15
3.3	Differential Pumping Stage	15
3.4	Main Chamber	16
3.4.1	Quadrupole Mass Spectrometer	16
3.4.2	Quartz Crystal Microbalance	17
3.4.3	Cluster Deposition Unit	18
3.4.4	Time of Flight Mass Spectrometer	19
3.4.5	Vacuum System	21
3.5	Scanning Transmission Electron Microscope Analysis	21
3.6	UV Spectrometer	23
4	Experimental Results	24
4.1	Time of Flight Measurements	24
4.1.1	Measurement of Helium Droplets	24

4.1.2	Monometalic Molecules inside Helium Beam	25
4.1.3	Bimetallic Molecules inside Helium Droplets	31
4.2	Temperature Dependent Analysis in a Transmission Electron Microscope	35
4.2.1	Ni-Au Clusters	36
4.2.2	Ni-Au Nanowire	40
5	Computational Method	43
5.1	Time of Flight Measurement	43
5.1.1	Mono Metallic Signal	43
5.1.2	Bimetallic ToF Signal	44
5.2	Diffusion in Au/Ni core shell structures	47
5.2.1	Principle	47
6	Conclusion	54
7	Appendix	55
7.1	Absorption Spectra of Cluster	55
8	Danksagung	60
9	Bibliography	61

List of Figures

2.1	Phase diagram of ${}^4\text{He}$ with respect to pressure and temperature	3
2.2	Different droplet formation behaviour of He	4
2.3	Size distribution of metal cluster crystal structures	7
2.4	Phase diagram of gold and nickel	9
3.1	Overview of the setup for the creation of helium nano droplets	10
3.2	Image of used and clogged nozzle plate	11
3.3	Schematic sketch for doping helium droplets	13
3.4	Picture of inside the Pickup chamber	14
3.5	Partial pressure of gold, nickel and copper	15
3.6	Helium spectra with impurity peaks	16
3.7	Piezoelectric crystal resonance frequencies	17
3.8	Sample holder for the TEM grids	19
3.9	Schematic sketch of a straight electron multiplier	20
3.10	Schematic sketch and TEM image of the used heatable TEM grid	22
4.1	Time of flight mass spectra for an undoped helium beam	25
4.2	Time of flight mass spectrum for helium beam doped with Cu	27
4.3	Time of flight mass spectra for a helium beam doped with Au	28
4.4	Time of flight mass spectra for a helium beam doped with Ni	30
4.5	Ionisation potential of nickel cluster	31
4.6	Time of flight mass spectra for a helium beam doped with Cu and Ni	32
4.7	Separated time of flight spectrum for nickel, copper and Ni-Cu doped helium beam	33
4.8	Heating curve for Au/Ni heating experiment	37
4.9	Overview of Ni/Au core-shell cluster	38
4.10	Three different core-shell cluster	39
4.11	Temperature dependent images for the Ni/Au core-shell cluster	39
4.12	HAADF image of core-shell nanowires	40
4.13	EELS and EDX spatial resolved measurements for Au/Ni cluster	42
5.1	Simulation of the nickel Time of flight spectrum	45
5.2	Simulation of the nickel Time of flight for a cluster of seven atoms	46

5.3	Simulation of the nickel/copper time of flight spectrum for clusters with seven atoms	47
5.4	Measurement method to analyse the core-shell cluster	48
5.5	Experimentally gathered intensity profile	49
5.6	Schematic 2-dimensional drawing of a spherical core-shell cluster	50
5.7	The fit of the observed density profiles to the cluster	52
5.8	Temperature dependent diffusion length	53
7.1	Absorption spectra of Ag nanowires	56
7.2	Absorption spectra of Au cluster	57
7.3	Transmittance of the used fused quartz	57
7.4	Mixed Ni and Cu Time of Flight spectrum	58

1 Introduction

Bimetallic nanoclusters have attracted recent attention in the last decades due to their unique physical properties. The potential applications of such materials cover a broad range from optics¹, catalysis^{2,3} to applications in medicine⁴. Magnetic-noble metal core-shell particles are especially interesting: the magnetic metal core provides a high magnetic moment, which can be used for medical applications such as DNA separation⁵, drug delivery and magnetic resonance imaging (MRI) enhancement⁶. Small particles of pure magnetic elements such as iron, cobalt and nickel are easily oxidised, a process which destroys most of their magnetic properties. However, their oxidation can be avoided by creating a shell with a noble metal, leading to a core-shell type structure. Gold seems to be particularly suitable because of its unique optical properties e.g. surface plasmon resonance⁷ and it offers adhesive layers for different biomolecules⁴ as well. All these attributes make the core-shell system Ni-Au a good candidate for being a biosensor⁸.

A whole series of unusual effects emerge at the nanoscale: negative magnetoresistance⁹, quantum conductance¹⁰ or ferromagnetism¹¹. Since fundamental dynamics of these systems are crucial to understand, many studies have been made to investigate different parts of the very nature of this topic^{12,13,14,15}. However, when investigating regimes in between the single atom and the bulk, their properties are heavily dependent on scale and the structure. Often chemical synthesis is used to create clusters within solvents. The downside of this kind of synthesis is, that the solution around the cluster is not completely inert and may change the clusters properties¹⁶.

A different approach is used for the synthesising of clusters within this thesis. Helium nano droplets were extensively utilised as an ultra cold inert matrix for the spectroscopy of atoms, molecules and small clusters. Having a very low temperature, the helium droplets also have the possibility of sequential doping, which makes them an ideal tool for designing desired cluster formations.

Within this thesis, two different types of measurements are discussed:

- Time-of-flight spectra of mono metallic and bimetallic clusters with up to 15 atoms
- Temperature resolved transmission electron microscopy of core shell clusters with a diameter below 10 nm.

The aim of these studies is to broaden the understanding of mixing between different elements at the atomic level and the nanoscale.

2 Theoretical Introduction

2.1 Helium

Helium is the second most common element in the universe and shows unique properties. Important to mention is, helium has two stable isotopes: ^3He and ^4He . ^3He shows fermionic behaviour, is extremely rare (only 0.000137 %) and needs a lower temperature for the superfluid state than ^4He . In this thesis, He and ^4He are used interchangeable unless otherwise stated.

Helium has a very high ionisation energy of (24.6 eV) and has a superfluid phase below 2.17 K at ambient pressure¹⁷. At this temperature, helium reaches the so-called lambda-point. In this phase, the thermally induced de Broglie wavelength becomes longer than the distance between the atoms. This results in the atoms losing their identity and this condensation can be described by a macroscopic wave function. In this state, the thermal conductivity approaches infinity, causing an evaporation of helium when approaching the boiling point. Furthermore, also the viscosity of the liquid approaches zero and several other unusual effects occur in this phase. Between 4.20 K and 2.17 K helium acts as a liquid. Helium also being a noble gas, it is very inert to chemical bonds with other atoms making He droplets an ideal matrix for atomic studies.

2.2 Helium Droplets Formation

Helium droplets are used for many purposes, e.g. cluster synthesis. These droplets are formed via adiabatic supersonic expansion. Highly purified helium expands through a nozzle (commonly $5\ \mu\text{m}$ in diameter), at a specific pressure ($p_{st} = 10\ \text{bar}$ to $50\ \text{bar}$) and very low temperature ($T_0 = 3\ \text{K}$ to $25\ \text{K}$) into high vacuum. Adjusting the pressure and the temperature, different kind of droplet formations can be realized:

1. Subcritical regime (I): $T_0 > 12\ \text{K}$ and $p_0 = 20\ \text{bar}$. Helium expands in gaseous form. During the expansion, the temperature drops linearly with pressure, down to the gas-liquid line. The helium condensates into droplets.
2. Intermediate regime (II): $9\ \text{K} < T_0 < 12\ \text{K}$ and $p_0 = 20\ \text{bar}$. The behaviour of the helium becomes unstable. The isentropes of the different temperature pass close

to the critical point.

- Supercritical regime (III): $T_0 < 9\text{ K}$ and $p_0 = 20\text{ bar}$. The helium forms a liquid already in the nozzle. The helium beam becomes liquid, the droplets form by fragmentation of the beam.

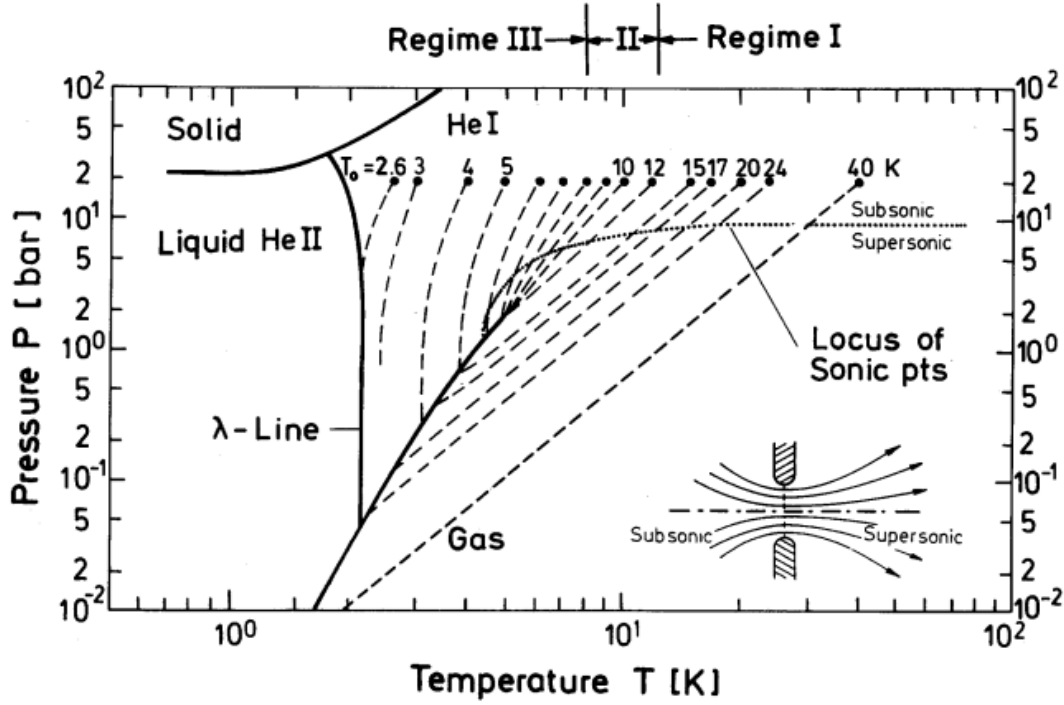


Figure 2.1: Phase diagram of ^4He over pressure and temperature. The dashed lines represent the isentropics of the helium beam expanding at 20 bar out of the nozzle and with nozzle temperature T_0 ranging from 2.6 K to 40 K. The expansion leads to a drop in temperature of the helium. As discussed in the enumeration above the different regimes are **Subcritical (I)**, **Intermediate (II)** and **Supercritical (III)**. This figure was taken from Ref. 18.

One anomaly of helium can be seen in Fig.2.1; Helium has no triple point but has an additional phase transition (indicated by the λ -line) from fluid He I to the superfluid state He II. The different regimes of droplets formation go along with different droplet sizes. The sizes change dramatically depending on the conditions of the helium droplet during creation. It is of great importance to know the conditions for changing the helium droplet size for the creation of nanostructures. Different kinds of measurement have been conducted^{19,20,21} resulting in Fig.2.2 .

A huge range of different droplet sizes is accessible by tempering the helium nozzle or changing the stagnation pressure.

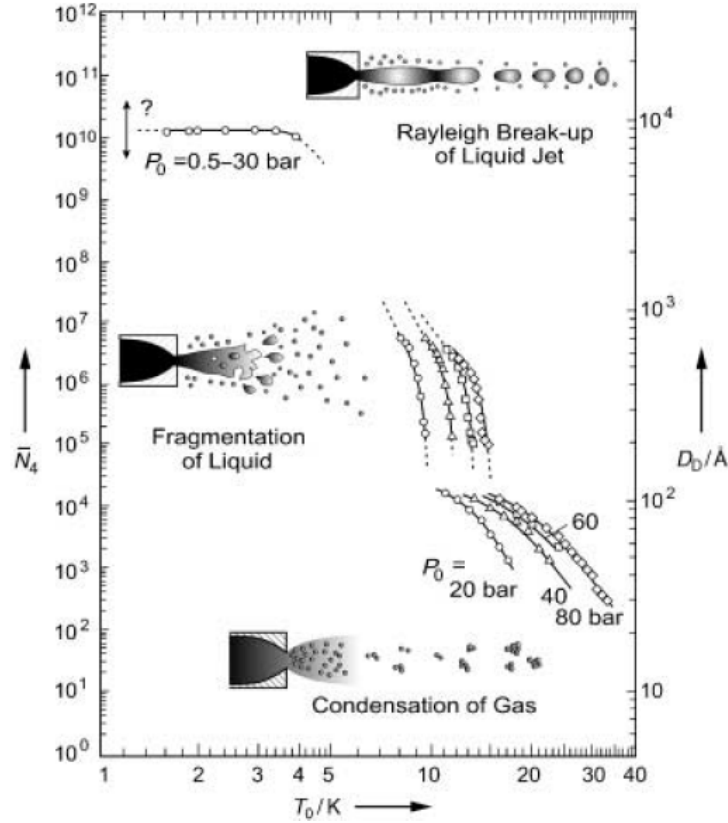


Figure 2.2: Overview of various regimes of droplet formations behaviour, depending on the pressure and the temperature. The three different mechanisms are closely related to the discussed mechanisms of En.2.2. This figure was taken from Ref. 17 .

2.3 Pickup of Foreign Atoms

Helium droplets have the ability to pick up every substance or foreign atom they touch. This leads to the possibility that various materials can be incorporated into the helium droplet. For small numbers of foreign atoms the pickup possibility can be determined as a Poisson distribution²²:

$$P_x(k) = \frac{x^k}{k!} e^{-x}, \quad (2.1)$$

here x is the average collision distance between the helium droplet and foreign atoms and k is the number of atoms picked up by the helium droplet. For this approach, the evaporation of helium during the pickup events is neglected. This evaporation takes place because of energies being transferred to the helium droplet. The binding energy of a helium atom to the droplet is 0.62 meV. As a rule of thumb it can be estimated that for 1 eV of energy around 1600 helium atoms are evaporated¹⁷. In the case of two or more foreign atoms being picked up these atoms can release binding energy. Additional

to the binding energy, the picked up atoms have a kinetic energy which results in an extra evaporation of helium. In conclusion, this leads to a total of ≈ 4800 helium atoms per silver atom ($E_{binding_{Ag}} \approx 3 eV$)²³. The evaporation cooling of the droplet takes place between 10^{-7} to 10^{-9} seconds.²⁴ There are also elements which are not incorporated into the helium droplet but appear to stay on the surface of the droplet, e.g. rubidium²⁵.

Helium Vortices

During the expansion of the helium through the nozzle at low temperature ($T_0 < 6 K$ at 20 bar) the helium beam undergoes a Rayleigh breakup. During this process, the liquid helium is in contact with the nozzle plate. Through this interaction, angular momentum is transferred to the droplet. During the expansion the droplet cools itself, by evaporation of helium atoms, down to $\approx 0.4 K$, crossing the transition point from normal fluid to superfluid state ($T_\lambda = 2.17 K$)²⁶. At the superfluid state, the vanishing viscosity prohibits the transformation of the angular momentum into solid body rotation. The conservation of angular momentum is preserved through the development of vortices. These vortices have each a quantum circulation θ . A vortex carrying more than one θ seems energetically unfavourable, leading to the generation of numerous vortices forming in a hexagonal shape²⁷. The number of vortices in a droplet is in the range of 150 to 200 vortices per droplets²⁸. Foreign atoms which are captured by the superfluid helium, are drawn towards the vortex cores because of a pressure gradient. This mechanism is used to create nanostructures of foreign atoms inside the helium droplet²⁹.

2.4 Time of Flight Measurements of Nano Structures

For analysis of small metal clusters, synthesised in helium droplets, time of flight spectroscopy was used. For the detection of helium or foreign atoms, electron impact ionisation was applied. The ionisation process is discussed here.

2.4.1 Electron Impact Ionisation

The droplet size of the helium is much bigger than the structures formed by the foreign atoms inside the droplet. For silver and gold this means that these structures are completely covered by helium.

For an electron within a helium droplet, the mean free path was calculated by Ellis *et al.* to be 2.59 nm for 40 eV³⁰. Gomez *et al.* estimated for an electron with 50 eV the mean free path to be 14 nm²⁰. The ionisation of a dopant is very unlikely to happen ($\approx 29\%$ for a helium droplet with $n = 3000$)³¹. Thus only the helium interacts with the

electrons. When an electron with an energy higher than 24.59 eV hits a helium atom it can be ionised. This process can be described with



In Eq.2.2 the ionisation of a helium atom by a high energetic electron is described. The resulting He^+ ion will perform a random walk. Helium having the highest ionisation energy of all elements, the ionisation energy of the dopant will always be smaller. If a charge transfer from the helium to the dopant occurs, energy is released. This leads to additional ionisation of dopant atoms or to fragmentation. The released energy will result in evaporation cooling of helium until the equilibrium droplet temperature of 0.4 K is reached again.

It is also possible that a high energetic helium atom transfers its energy to a dopant atom leading to an ionisation of the dopant if the energy is higher than the ionisation energy of the dopant³². If there is no dopant inside the droplet, the charge hopping can go on until a dimer He_2^+ is formed. This happens statistically after 11 hopping events³⁰.

2.5 Characteristics of Cluster

Clusters are the centre between atoms and bulk materials. The forces inside the small metal cluster are primarily acting like covalent bonds. Not before the clusters are getting bigger, the binding characteristic changes more to metal-like behaviour. Many properties like the binding energy or the ionisation potential are cluster size depended. There are also different kinds of clusters in which the type of bonding varies. The Van der Waals clusters primarily have lower energy bonds than metal clusters, because of their name giving bond type. This type of cluster also can be synthesised in liquid helium droplets³³.

2.5.1 Crystal Structure of a Cluster

Inside the ultra cold helium droplets, the foreign atoms are conglomerated at the quantized vortices. On this small scale, different crystal structures for the clusters become possible. For the minimum of the energy, the icosahedral (Ih) structure is preferable for small cluster, decahedral (Dh) structure for intermediate clusters and face-centered (fcc) structure for big clusters³⁴. For small clusters, the Ih is favourable because it reduces the surface energy at the price of higher inner strain. When the cluster gets bigger, the inner strain rises and the Ih structure is disfavoured. This behaviour changes for different kinds of synthesis types, like gas aggregation or via helium droplets³⁵. Different symmetries like Ih, Dh and fcc structures have been published for deposited clusters, with helium droplets as synthesis mechanism³⁶. A full investigation was carried out by Volk *et al.* where different high-resolution transmission electron microscope (HRTEM) images were analysed³⁶. The results are shown in Fig.2.3 .

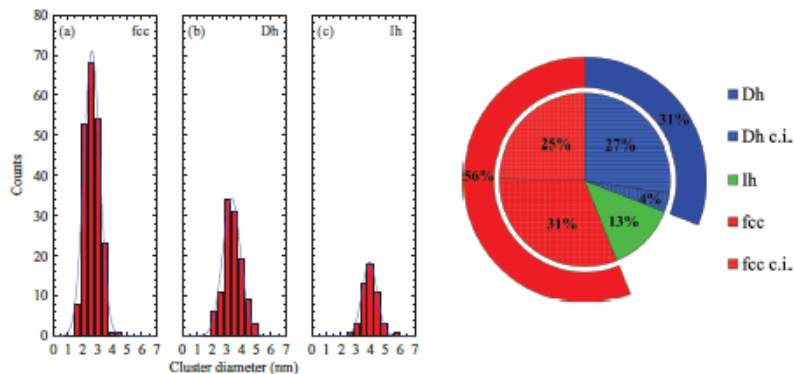


Figure 2.3: The size distribution of the different structures are displayed on the left side. Here the histograms were fitted gaussians displayed for (a) fcc ($\bar{d} = 2.63(5)$ nm, $n \approx 550$), (b) Dh ($\bar{d} = 3.34(7)$ nm, $n \approx 1150$) and (c) Ih ($\bar{d} = 3.93(2)$ nm, $n \approx 1870$). On the right side, the ratios of the structures are shown in dependence of all investigated clusters. This analysis was carried out on silver clusters produced in a helium droplet machine. This figure was taken from Ref. 36 .

as one can observe from the results of Fig.2.3, the fcc structure seems more favourable for small cluster sizes than Dh and Ih for clusters synthesised in helium droplets. This circumstance shows that for small clusters a phase transition upon the impact on the carbon grid seems possible³⁷.

2.5.2 Deposition on Substrate

The helium droplets leaving the nozzle have a velocity of up to $300 \frac{m}{s}$. The droplet beam is terminated on a Transmission Electron Microscope (TEM) grid for analysis of the dopant nanostructures within. One may think that the kinetic energy of the clusters inside the helium droplet may be high enough to break bonds and therefore just fragmented structures are visible in the TEM. The influence of the kinetic energy will be briefly discussed here.

The doping process itself does not change the velocity of the droplets significantly, resulting in a kinetic energy per atom of ≈ 0.05 eV for small clusters. For gold, the binding energy is ≈ 3 eV, which is 2 magnitudes higher, thus there is no break up of nanostructures to expect. This regime is called "Soft landing"³⁸.

For bigger nanostructures the total kinetic energy can pass the binding energy of the atoms at the impact. This may lead to a fragmentation or deformation of the bigger nanostructures at impact. It is also possible that, if the binding energy of the substrate to the nanostructure is very high, the released binding energy can lead to fragmentation or phase transition.

While the cluster is surrounded by liquid helium, the helium will absorb some of the energy released during the impact by evaporation cooling. The cooling rate of suprafluid helium is $10^5 \frac{K}{ns}$ ^{39,40} meaning that a significant amount of energy is carried away.

2.6 Alloys

For mixing two metals together at a macroscopic scale many parameters must be considered. Especially for different compositions of metals, different kinds of mixing behaviours are observable. Alloying can be described by the change in the Gibbs free energy⁴¹. For a material containing two elements, this can be described as:

$$\Delta G_{Mix} = x_A \Delta G_A + x_B \Delta G_B + R(x_A \cdot \ln(x_A) + x_B \cdot \ln(x_B)), \quad (2.3)$$

where ΔG_{Mix} is the total value of the Gibbs free energy of the alloy, x_A and x_B are the amount of element A or B on the mixed solution and ΔG_B and ΔG_A is the Gibbs free energy of an alloy when just an additive mixing is assumed. The third term describes the mixing entropy of element A and element B. This approach is usable for macroscopic alloying processes. When approaching the nanoscale Eq.2.3 is not applicable, because of surface effects⁴². At this scale, the energies for each bond differ, from the bulk values. This mechanism gives rise to different phenomena at nanoscale⁴³. Inside the super cold helium droplets, the foreign atoms are conglomerated at the quantised vortices, forming different kinds of nanostructures. It is also possible to dope more than one kind of atoms inside the helium droplets³⁸. By doping two different kinds of foreign atoms inside the helium droplet so-called "core-shell" structures can be created. Having two elements in a superfluid helium droplet opens the possibility to investigate the alloying of different atomic species. A macroscopic phase diagram can be seen in Fig.2.4 .

For very low doping rates of foreign atoms, it is also possible to investigate alloying of compounds with low atomic number⁴⁵. Analysing the Time of Flight (ToF) signal one can see for specific complexes the signal is higher. Within this thesis, the alloying process between gold and nickel is examined and the diffusion length is estimated.

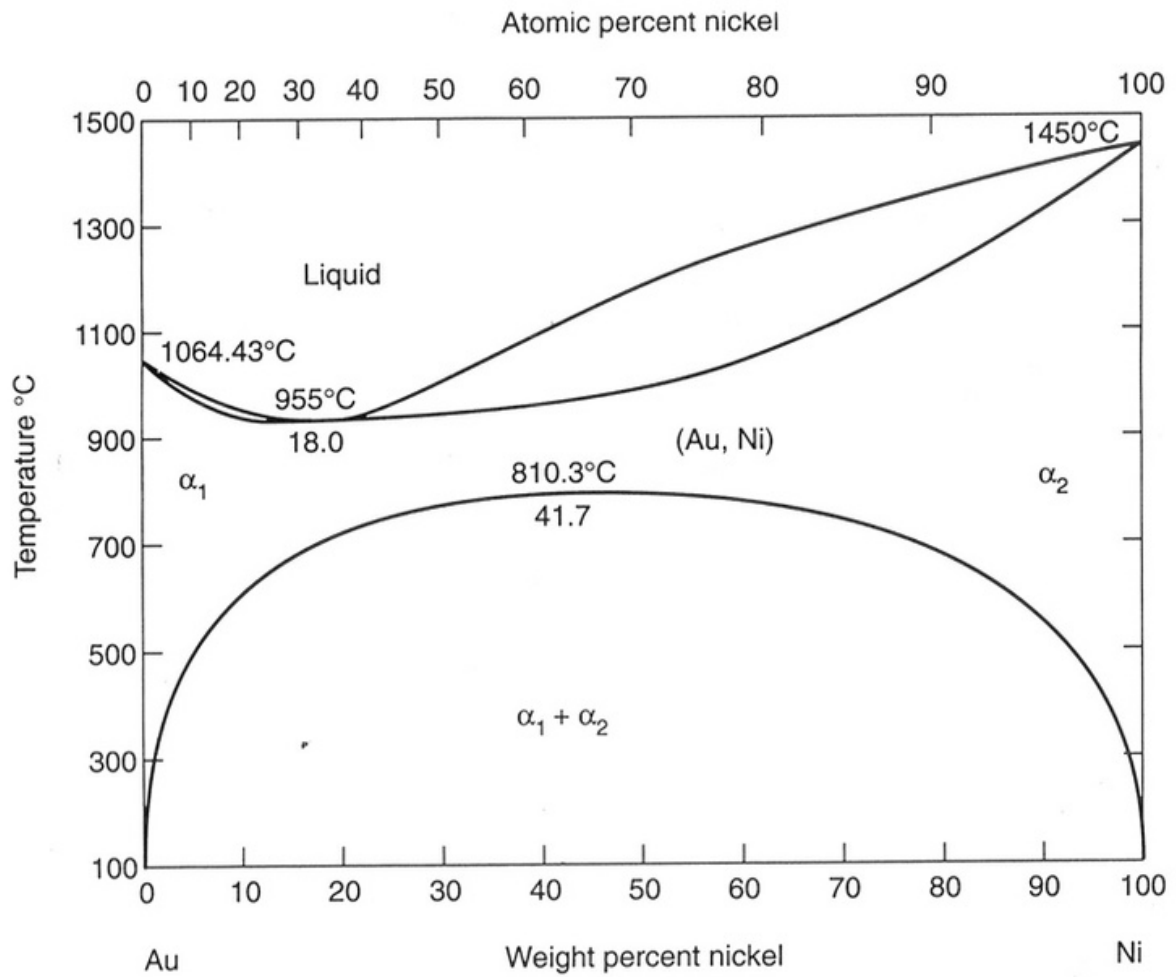


Figure 2.4: Macroscopic phase diagram of gold and nickel. Before reaching the liquidus line both elements have a separate phase. The first alloying of this bimetallic system appears at 955°C. This figure was taken from Ref. 44 .

3 Experimental Setup

In this chapter, the apparatus on which the clusters for all measurement for this thesis were produced, is illustrated. The vacuum system of the apparatus consists of four different chambers, which are described separately. The most important tool was a Time of Flight mass spectrometer which was used to measure large atomic clusters *in situ*. For smaller masses, a quadrupole spectrometer was used. Further, two heating cells were used to evaporate different materials. To measure the deposition of the helium droplet beam a quartz crystal microbalance was used. A schematic sketch of the experimental setup is visible in Fig.3.1 . All parts of the apparatus are described below.

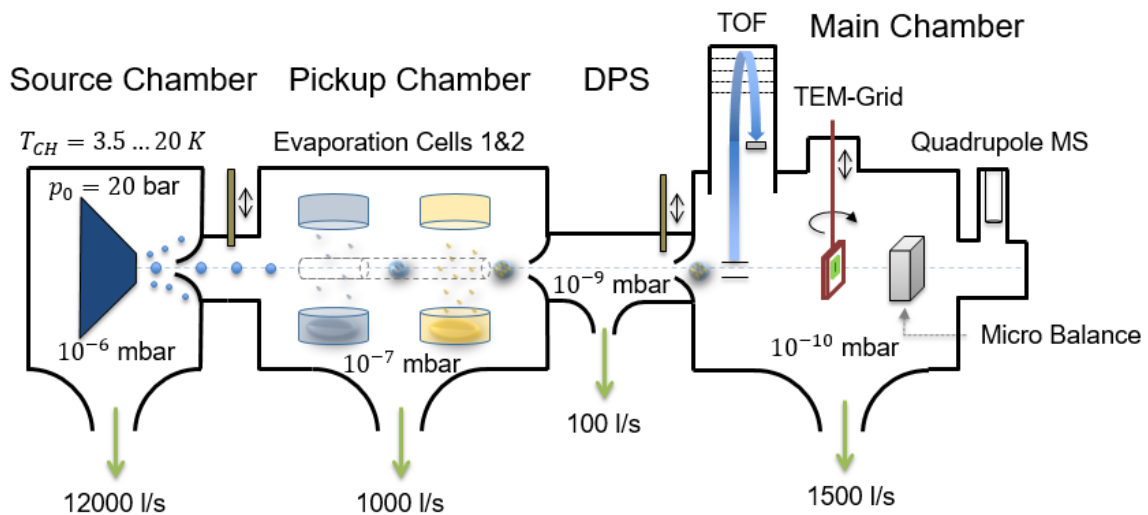


Figure 3.1: A schematic sketch of the setup for helium droplet machine. The setup can be divided into four chambers. In this sketch, the different analytic hardware is also included. The vacuum system is described below for every chamber separately, here the effective pump volumes are displayed. This figure was taken from Ref. 46 .

3.1 Source chamber

Besides the vacuum system, the Source chamber also contains the cold head, which is essential for the creation of the helium droplets.

3.1.1 Coldhead

The cold head used was a Sumitomo RDK-408D2. The cooling takes place over two different cooling stages. In Sec.7 the cooling capability of this cold head is shown, for both cooling stages. The helium beam is produced by expanding helium, with a stagnation pressure p_{st} , through a nozzle plate (2 mm diameter, 0.6 mm thickness, Günther Frey GmbH) with a nominal diameter of $5\ \mu\text{m}$. The nozzle plate can be seen in Fig.3.2 and is made of a Platinum/Iridium alloy. During this expansion, the ultra pure helium (purity of 99.9999%) undergoes a supersonic expansion.

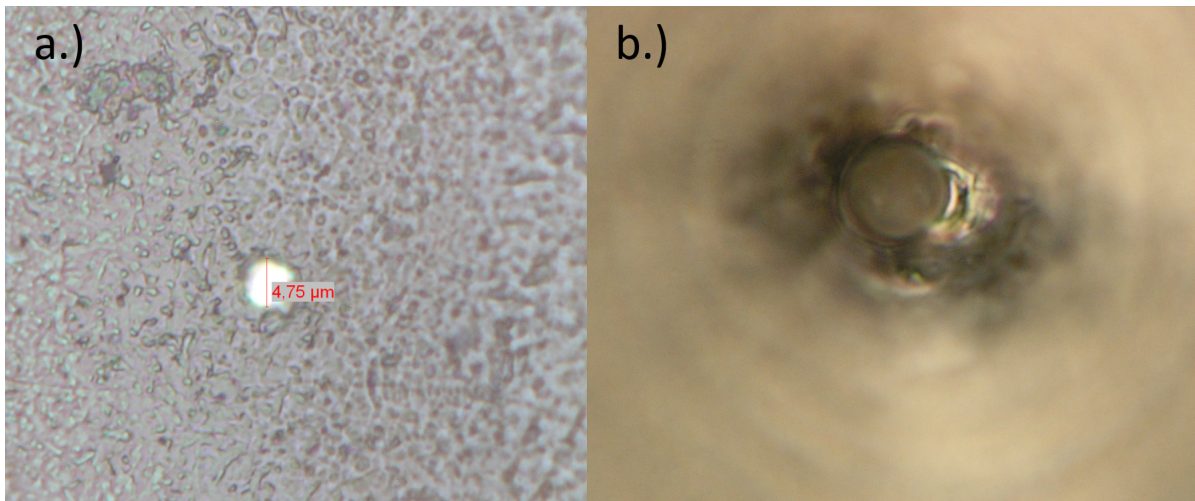


Figure 3.2: Left: Image of the used nozzle plate. The measured diameter is $4.75\ \mu\text{m}$.
Right: Image of a nozzle plate clogged by an oil droplet. For imaging, an optical microscope was used.

The nozzle plate is mounted onto the second cooling stage of the cold head. The whole cold head is surrounded by a radiation shield (oxygen free copper) which is connected to the first cooling stage. This shield is additionally covered with an insulating film, which is strapped around. With $p_{st} = 20\ \text{bar}$ a temperature of $3.8\ \text{K}$ is achievable. The cold head is mounted onto the chamber by a tripod. This construction is used for the alignment of the helium beam within the chamber. Although this gives the possibility to change and manipulate the position of the cold head, it is a very rudimentary method. The nozzle position can be optimised by changing the direction of the cold head and looking at the different pressures of the system. When an abrupt rise in the Pickup chamber occurs,

one can be sure to aim through the first skimmer of the Source chamber. This skimmer is mounted to collimate the helium beam. The skimmer is mounted ≈ 2 cm after the nozzle and has a diameter of $400 \mu\text{m}$.

3.1.2 Vacuum system

The vacuum system of the Source chamber was built to fulfill special conditions. During the measurement p_{st} is kept constant and therefore the vacuum system has to hold low pressure even while helium expands in the chamber. This demand results in using pumps with very high effective pumping rates. On the Source chamber three different kinds of pumps work together to obtain the desired pressure of $< 10^{-4}$ mbar. The starting of the vacuum system is a rotary vane pump of the type E2 M 80 from Edwards. This pump functions as a fore pump for a roots pump. The roots pump is an Edwards EH 250. After the roots blower, an oil diffusion pump is mounted. This pump is a Leybold DI 1200. The effectively pumped volume for this pump is $12000 \frac{\text{l}}{\text{s}}$ making it ideal for the use in this chamber.

Using an oil diffusion pump results in one disadvantage: The resulting oil droplets could clog the nozzle. This would lead to a total failure of the helium beam resulting in a time intensive change of the nozzle plate. Therefore p_{st} is always kept above 5 bar to prevent the nozzle from clogging. In Fig.3.2 a picture of a nozzle which was clogged by an oil droplet is visible. Besides special copper fans are installed between the oil diffusion pump and the chamber to also prevent oil droplets coming near the nozzle.

3.2 Pickup Chamber

Inside the Pickup chamber the evaporation elements are located. During the flight of the helium droplets through this chamber, foreign atoms are picked up by the helium droplets. This process can be seen in Fig.3.3.

3.2.1 Evaporation cells

To dope helium droplets with foreign atoms, the partial pressure of the desired element has to rise significantly. This can be achieved through heating the element and therefore raising the vapour pressure. To achieve this, often temperatures near the melting point have to be attained. The crucible used to heat all the elements was a Ted Pella Style 6, Alumina Coated Tungsten Wire Basket, ID 0.900", 768 Watts. This kind of crucible consists of an aluminium coated tungsten wire. This small basket makes it possible to use grains or powder because it has a completely closed bowl and can be heated up to 1800°C making it possible to evaporate nearly all elements of interest.

During the experiments, the helium beam is hit by the evaporated atoms from one side

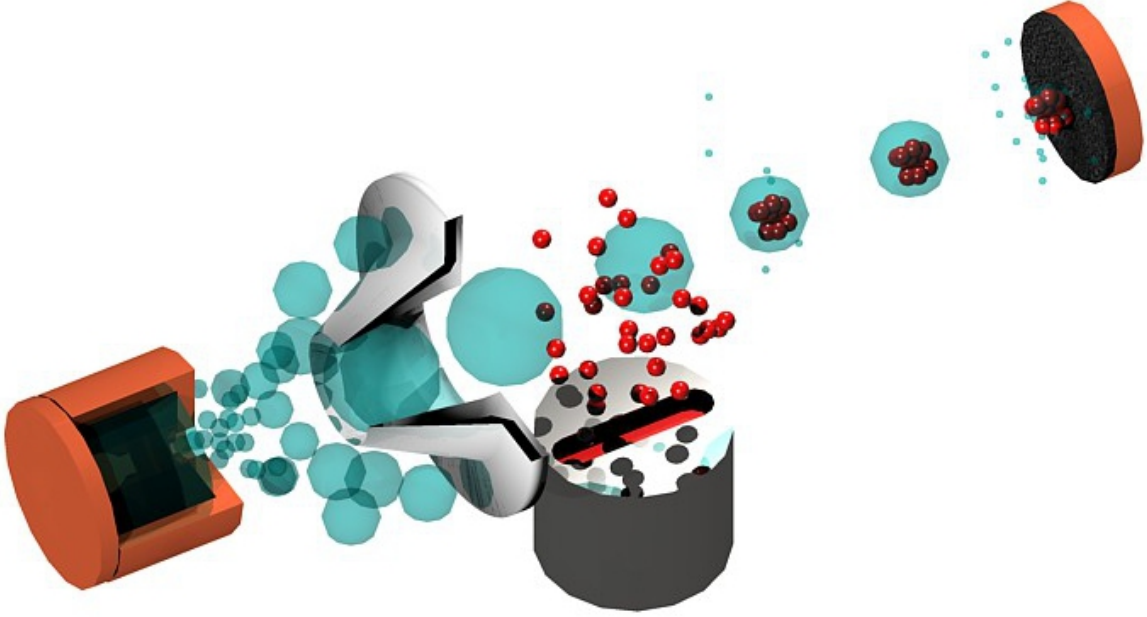


Figure 3.3: Example of the doping process of helium droplets by foreign atoms. In this illustration, a crossed beam setup is displayed. After the pick up the deposition of a target is shown under soft landing condition. This figure was taken from Ref. 31 .

with an angle of 90° . The momentum transfer through one basket leads to a deflection of the helium beam. For bigger cluster deposition experiments the atoms, coming just from "one side" changed the direction of the helium beam significantly, making it impossible to guide the helium beam into the main chamber. To prevent a significant deflection of the beam, a second crucible was mounted above the other one (closed evaporation cell). The baskets are heated by an external electric power supply, which is controlled by a software. The software uses the resistance of the crucible to determine the current temperature. For the heating control, the following simple model for the resistance was used:

$$R_T = R_{20} \cdot (1 + 0.0044 \cdot (T - 20)) \quad (3.1)$$

with R_T being the resistance at a temperature T , R_{20} being the resistance at the temperature of 20°C . For the current supply of the crucibles, wires with a cross-section of more than 25 mm^2 were chosen to reduce the resistance of the wires. The baskets are parallel connected resulting in both having the same temperature. The principle of the closed evaporation cell is as follow: in the lower basket, the pure element is deposited before the experiment. Due to the high temperature, the rate of atoms evaporated from the element in the lower basket starts to rise by many orders of magnitude. The evaporated atoms from the lower crucible are either picked up by a helium droplet or move to the

top basket where they are reflected and move down again through the beam line of the helium or being again reflected from the lower crucible and so forth. The configuration of within the Pickup chamber is visible in Fig.3.4.

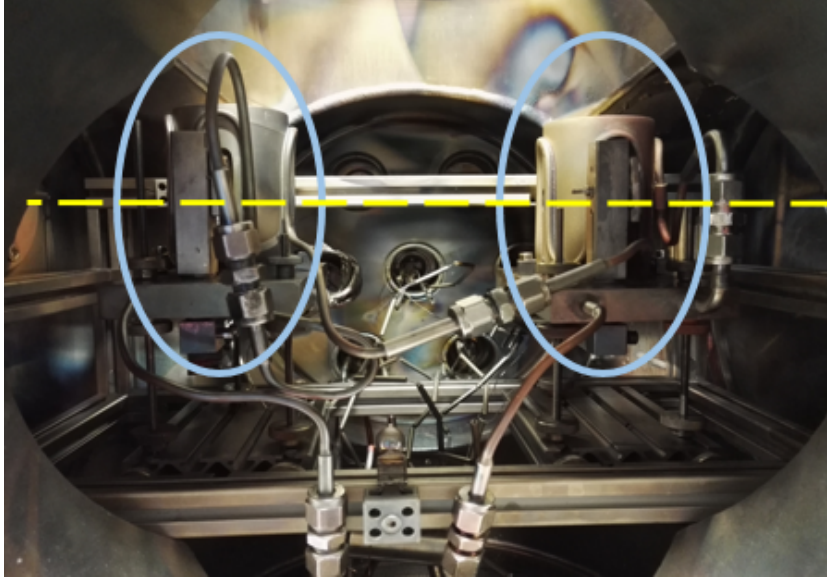


Figure 3.4: Picture taken of the inside the Pickup chamber. The two ovens are highlighted by a blue elliptic shape. The flying path of the helium droplets is marked by a yellow line.

The cooling shield prevents other parts of the chamber of being exposed to the high temperatures of the crucibles. The crucibles are under a heating shield, which is water cooled. The cooling lines inside the Pickup chamber are connected via Swagelok. For the alignment of all parts of the evaporating cells, the whole setup is mounted on tripods. The size of the chamber enables to mount two evaporation cells.

Partial pressure

Above, the partial pressure of the different elements was mentioned. To have a better understanding of the temperatures used during the experiments and to which partial pressures they correspond, a short discussion is presented here. Vapour pressure in the range of 10^{-10} Pa to 10^{-2} Pa can be described by using the following equation:

$$\log(p) = 5.006 + A + B \cdot T^{-1} + C \cdot \log(T) \quad (3.2)$$

here T is the temperature in K and A , B and C are constants. The values A , B and C were taken from Ref. 47. Eq.3.2 can be used to describe the partial pressure of solid and liquid metals and can reproduce the observed vapour pressure to an accuracy of 5% or better. For the experiments presented later on, three different elements are most

important: gold, nickel and copper. The resulting graph for the three elements can be seen in Fig.3.5.

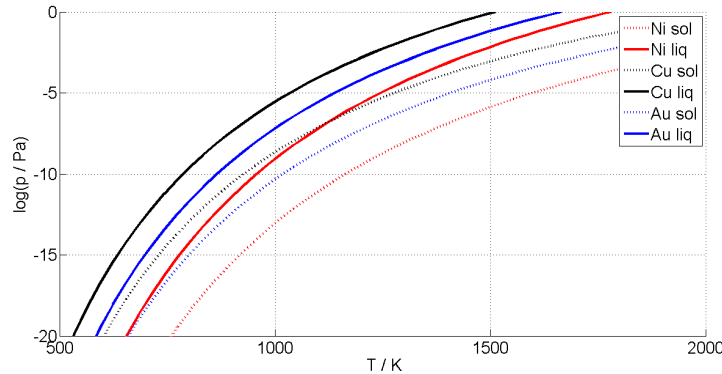


Figure 3.5: The partial pressure in dependence of the temperature in K of gold, nickel and copper. Here the partial pressure for the solid phase is marked by a dotted line, and the partial pressure for liquid phase is marked with a continuous line.

3.2.2 Vacuum system

Coming from the Source chamber the beam has to pass a skimmer with a diameter of $400\ \mu\text{m}$. In the Pickup chamber a total pressure of $\approx 5 \cdot 10^{-7}$ mbar is achieved during experiments. The vacuum system for this chamber contains three different pumps. For the fore vacuum a rotary vane pump of type Trivac D 8 B from Leybold is used. As main pump a turbo molecule pump HiPace from Pfeifer is used; reaching a final pressure in the high 10^{-7} region. As additional pump a cooling trap is installed in the Pickup chamber. Here liquid nitrogen is used to cool down a cylinder shape inside the chamber. Additional heating elements for the bake out of the chamber are placed inside. Three halogen lamps are mounted inside the chamber to reach temperatures of $\approx 100^\circ\text{C}$ for bake outs.

3.3 Differential Pumping Stage

Between the Main chamber, and the Pickup chamber another chamber is mounted. Coming from the Pickup chamber, the helium beam passes through a skimmer with a diameter of 2 mm to enter the differential pumping stage. This chamber is installed to smoothen the high pressure gradient from the main chamber (10^{-10} mbar) to the Pickup chamber (10^{-7} mbar). The pressure here is in the range of 10^{-8} mbar during measurements.

3.4 Main Chamber

Coming from the differential pumping stage, an aperture is mounted before the main chamber. In this chamber several analytic diagnostics are installed. Therefore, an oil-free fore-pump is used alongside three turbo molecular pumps. Although all pumps are oil free, helium droplets still transport oil molecules into the main chamber. Typical peaks of pumping oil can be seen in the time of flight spectrum at $m = 276$ u and $m = 390$ u. A complete helium spectrum including these both peaks is visible in Fig.3.6 for a cold head temperature of 9.5 K and a $p_{st} = 20$ bar.

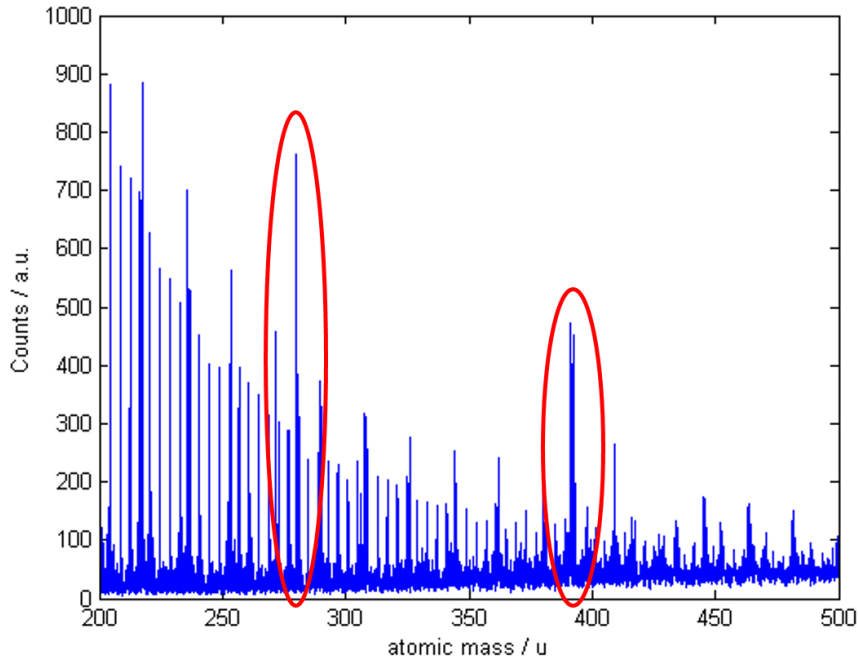


Figure 3.6: Helium mass spectrum for a cold head temperature of 9.5 K and $p_{st} = 20$ bar. The peaks of oil contamination are clearly visible and are marked by red ellipsoids.

3.4.1 Quadrupole Mass Spectrometer

The QMS mounted on the main chamber uses a Faraday detector type and can detect masses up to 200 amu. It is mostly used in the interval from 0 to 50 amu as a residual gas analyser, especially for the detection of ^4He . In this setup the QMS is mounted off beam axis, to detect the total current of ^4He inside the chamber. It is used to monitor the attenuation of the helium beam during measurements. Because of the evaporation cooling, the helium flux will decrease if the doping rate rises. For the detection of higher

masses, a Time of Flight spectrometer is used (described in Sec.3.4.4). Both signals have shown good agreement with each other, making both a reliable measurement of the helium flux inside the beam. During the doping of the helium beam, the time dependent signal of ${}^4\text{He}$ is a reproducible value for different parameters.

3.4.2 Quartz Crystal Microbalance

The determination of the deposition time of clusters onto the TEM grids is challenging. When the surface coverage would be too low, it is hard to observe enough clusters for a sufficient evaluation. The desired amount of coverage is achieved by measuring the mass flow, which is transported by the liquid helium beam. The measurement itself is challenging because the mass flow is very small (between $10^{-3} \frac{\mu\text{g}}{\text{cm}^2\text{s}}$ to $10^{-6} \frac{\mu\text{g}}{\text{cm}^2\text{s}}$). For this low regime of mass deposition, a quartz microbalance is used. The principle of using an oscillating quartz for weighing thin films was proposed by Sauerbrey in 1959⁴⁸. In the original paper Sauerbrey had the idea, that for an oscillating quartz, the frequency does not only dependent on the structure of the quartz itself, but on the mass covering the quartz. If a voltage is applied to a piezoelectric crystal, the crystal changes shape proportional to the applied voltage. Different resonance frequencies for piezoelectric electric crystals are shown in Fig.3.7.

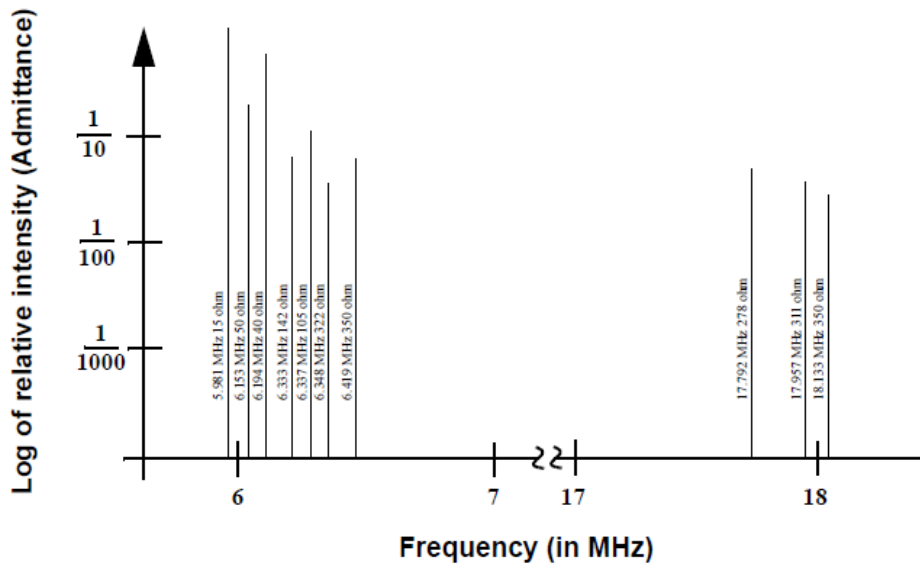


Figure 3.7: Intensities of resonance frequencies for a piezoelectric crystal. This figure was taken from Ref. 49 .

For some discrete frequencies of applied voltage, a very sharp resonance frequency of the crystal can be observed. For measurements within this work, the interval of frequency was kept between 4 Mhz and 6 Mhz. The additional mass on the quartz

results in a decrease of the oscillating frequency. This drop in frequency is related to mass deposited onto the quartz. This can be calculated with the Sauerbrey-equation:

$$\Delta f \approx -\frac{2f^2}{Z}m \quad (3.3)$$

where f is the resonance frequency, Δf is the change in frequency due to mass deposition, Z is a constant and m is the deposited mass. Important for this simple form is that the temperature of the quartz is constant. In this setup not only the piezoelectric element has to be temperature stabilised but also the electronics need a constant temperature. The temperature of the electronics as of the crystal are kept constant due to Eurotherm controllers, which keep the electronics outside the chamber at a constant temperature of 40 °C and the crystal inside the chamber at a temperature of 50 °C. The controllers enable a stability of the microbalance setup of ± 0.02 °C. Additionally, the air condition of the laboratory was equipped with a controller, to achieve a constant temperature within the room. This controller regulates the time in which the cooling is activated. Even when this cooling stage is not sufficient, leading to a rise in the temperature of the room, only a long time drift of the deposition would appear and would not impact the measurement of the mass deposition rate significantly.

The use of a quartz crystal gauge not just enables the measurement of deposition rates through helium droplets, but also a mass gain, e.g. through the measurement of the oxidation of clusters on the quartz. For this experiment, nanostructures are deposited onto the microbalance and then the vacuum system is vented with oxygen. Through an oxidation effect, a significant mass gain onto the microbalance can be observed. The deposition rate is achieved by the deposition of clusters. The crystal has to be changed for different oxidation experiments, to ensure that only the mass gain of the deposited material is measured.

3.4.3 Cluster Deposition Unit

For the deposition of clusters onto TEM grids special specimen holders are mounted inside the main chamber. Movement around six different axes is possible. The x-,y- and z-position stays the same during most of the experiments. By rotation alongside the vertical axes, it is possible to quickly insert or remove the specimen into or from the helium beam. The many possibilities of changing the position in the vacuum chamber also make it easier to change and reattach the sample holder through the side flange, making the handling easier. When venting the chamber only dry nitrogen is used. By being very quick in detaching the sample holder, the time at ambient condition can be limited to a few seconds.

In many experiments, it brings great advantage if more than one sample is prepared. The specimen holder has two separate positions for holding TEM samples, making it

possible to prepare two specimens, changing between them by just rotating along the axis of the helium beam. The whole specimen holder contains roughly two parts: one sample holder which can be turned in the above-described ways and one copper plate. In Fig.3.8 the plate is displayed. Additional to the two drilled hole where the TEM grids can be fixed, another hole which is used for fused silica substrates is visible.

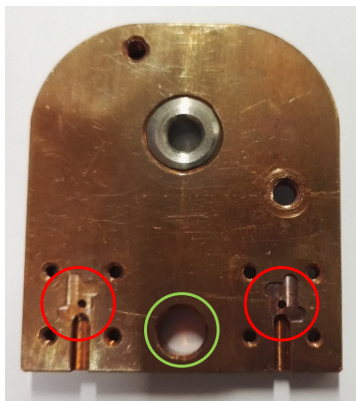


Figure 3.8: A photograph of the copper plate. The red circles mark the places where the TEM grids are mounted and the green circle marks the hole which is used for the deposition on fused silica.

3.4.4 Time of Flight Mass Spectrometer

For all mass spectroscopy measurements in this work a Time-of-Flight spectrometer RFT50 with electron impact ionisation and 20 kV post acceleration is used. For the generation of ions, electron impact ionisation was used. In the following section, a short overview over the rudimentary principle of a Time-of-Flight mass spectrometer (ToF) is given.

Impact Ionisation

For the ionisation, electrons from an electrically heated filament are used. These electrons then pass through a known potential U_{tof} giving them the energy $E_e = eU_{tof}$. When an electron hits an atom and the ionisation energy of the atom is below E_e , the atom will lose one electron and becomes a positively charged ion. To raise the cross section of each electron, magnets are installed. The constant magnetic field will lead to a spiral trajectory of the electrons, resulting in a longer path in the ionisation zone of the ToF. This leads to a higher density of ions.

Ion Extraction

After the ionisation, the ions are extracted from the ionisation volume into the flight tube. This is the result of two electrodes, repeller and extractor. The repeller has a positive potential and the extractor a negative potential. This leads to an ionisation volume at ground potential. Assuming that every ion has one positive charge, every ion gains the same kinetic energy, because of the applied electric field. The velocities of these ions can now differ from each other, because of different masses. This leads to different times for the ions to pass the flying tube³¹.

Detection of Ions

For the detections of ions, a 3-stage Multi Channel Plate (MCP) is used. A MCP contains an array of miniature electron multipliers, aligned parallel to each other. The amplification of electron multipliers is typically between 10^4 and 10^7 ⁵⁰.

Important for the MCP is that all arriving ions are detected. To improve the measurement, the MCP plate is slightly tilted towards the flying path of the ions. When an ion now hits the MCP with sufficient kinetic energy, an electron is knocked out of the plate. A voltage is applied to the electron multiplier to accelerate these electrons towards the wall of the channel. On the wall multiple second electrons are knocked out and an electron avalanche effect is generated. This effect can then be measured as a current between the faces of the MCP. After a detection of such a cascade, the detector needs some time to regenerate before another event can be measured. This time is in the order of 10^2 ps⁵⁰. A schematic sketch of a MCP is shown in Fig.3.9. The detector

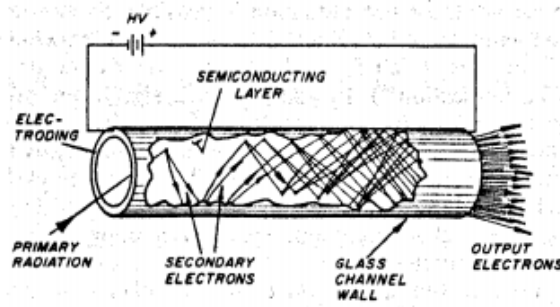


Figure 3.9: Schematic sketch of the creation of the second electrons within a straight electron multiplier. This figure was taken from Ref. 50.

with which every measurement was made, was a Multiscaler (Fast P7887) with a time resolution of 250 ps. If during one time step, more than one ion hits the plate, the signal appears to be saturated. It is important to mention that, when the signal is saturated, the MCP can be destroyed. To reduce the saturation of the sensor, a mass filter can be turned on. This leads to a deflection of the light ions away from the detector, thereby

they do not contribute to the spectrum, reducing the total signal. With this method, a significant reduction of the signal can be achieved and a MCP can be saved from critical damage.

For further readings and also for calibration note for the current setup, the reader is referred to Ref. 31.

3.4.5 Vacuum System

The pressure within the main chamber after bake out is $\approx 10^{-10}$ mbar. This low pressure suits the different measurements within the chamber. To reach this significant pressure region, the roots blower and a TMP pump are used to provide the fore-vacuum for the chamber. Due to the great distance between the main chamber and the fore-vacuum pumps the line loss of the fore-vacuum is very high. Therefore, to provide a sufficient vacuum a TMP had to be mounted in the fore-vacuum line, to provide the desired fore-vacuum pressure. A pressure of ≈ 1 mbar is achieved before the main TMP. To achieve the desired pressure in the main chamber three different TMP's are used, resulting in a total effective pumping speed of $1200 \frac{l}{s}$. With these vacuum pumps, a pressure of $\approx 10^{-8}$ mbar can be sustained during measurements with very high helium beam intensities.

3.5 Scanning Transmission Electron Microscope Analysis

High demands were required for the analysis of structures with the size of ≤ 10 nm. Only a few measurement techniques are capable of having this high resolution. For the experiments presented in this work, a Scanning Transmission Electron Microscope (STEM) was used. Especially the high resolution was a key factor for the highly successful measurements.

A detailed description of a STEM can be found in Ref. 51. In short, electrons are emitted from a cathode by heat or by field emission. Through a system of electromagnetic lenses, the beam can be focused on the specimen. Here, thicknesses of up to 100 nm of the specimen can be penetrated by the electrons. The resulting pictures are then enlarged by a system of electro-magnetic lenses and then projected on a fluorescent screen or CCD chip for digitalisation. During the picture creation, the elastically scattered electrons are important whereas for analytical principles the inelastically scattered electrons are analysed.

The specimens were analysed in a probe-corrected FEI Titan3 G2 60-300 using the high angular annular dark field (HAADF) recording technique. The acceleration voltage in-

terval from 60 kV to 300 kV allows optimising the voltage depending on the material examined. It was equipped with a Gatan Quantum energy filter for electron energy loss (EELS) and four-quadrant energy dispersive X-ray spectroscopy (EDX) detectors (FEI Super-X) for the determination of material composition. As an electron source a Schottky emitter was used, generating a high electron current. During the measurements, atomic-resolution was achieved. The special TEM grid Nano-chip XT Carbon from DENSSolution is a new generation of TEM grids. It can be heated up to 1300 °C with heating ramps of $200 \frac{^{\circ}\text{C}}{\text{ms}}$ and the specifications of this chip stay constant within 5 %. This new kind of grid enables the observations of *in-situ* temperature driven phenomena in STEM, leading to a breakthrough in new measurement possibilities.

The idea behind this new chip is that a heating helix out of tungsten is placed onto the grid. This helix has four connection sections, with which the current and the resistance are measured. With this information, it is possible to determine the temperature of the helix. For heating, a current is applied to the helix. In the spaces between the helix, windows made out of thin films of amorphous carbon allow the observation. A schematic sketch and an image, taken with a STEM, are shown in Fig.3.10.

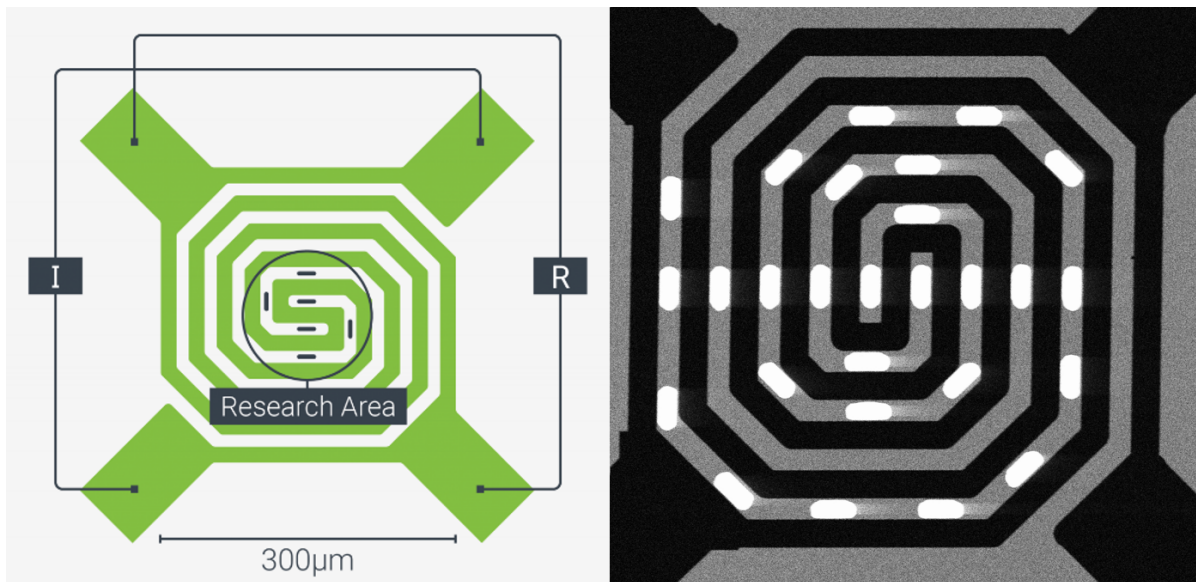


Figure 3.10: Left: Schematic sketch of the Heating TEM grid from DENSSolution. The four contact zones are labeled. The sketch on the left is taken from Ref. 52. Right: The image was taken from the heating chip. The white region marks the carbon film on which the measurement takes place.

3.6 UV Spectrometer

During this work, experiments, in which clusters of different elements were deposited onto a fused quartz plate (Corning 7980) and the absorbance was measured in a spectrometer, were made. For an absorbance spectrum, a UV-1800 Shimadzu spectrometer was used. Two different light sources were used: for wavelength higher than 340 nm a tungsten wire and for wavelengths below 340 nm a deuterium lamp. The range of measurements starts at 190 nm and ends at 1100 nm with a 0.1 nm step size.⁵³ The wavelength for the measurement was mostly in the visible and UV regime. This spectrometer uses two specimens for a measurement. One of them serves as reference and therefore nothing is deposited onto it. Due to the difference in the absorbance between both plates, the resulting changes through the deposited nanostructures are visible. With this technique, it is possible to eliminate absorbance from the fused quartz itself. The used fused quartz has a ≈ 0 % absorbance over a wide range. However, below 300 nm the absorbance of the quartz rises, making meaningful measurements impossible⁵⁴. The transmittance of the fused quartz from 100 nm to 5000 nm is shown in the appendix. The results of these measurements are beyond the scope of this work, which is why the results are shown in the appendix. The absorbance of gold and silver nanostructures have been measured as an outlook towards future projects.

4 Experimental Results

In this section, the performed measurements are presented. All measurements can be roughly divided into two sections: Time of Flight (ToF) measurements and temperature dependent analysis with a Transmission Electron Microscope (TEM). The experimental principles and configurations during ToF measurements of helium droplets are discussed in Sec. 4.1.1.

Mass spectra of monometallic clusters inside the helium beam are shown in Sec. 4.1.2. Mass spectra of Cu-Ni clusters in the helium beam are presented in Sec. 4.1.3. Measurements of temperature dependent diffusion lengths of Au-Ni core-shell clusters are shown in Sec. 4.2.1. Analysis of the temperature dependent behaviour of core-shell nanowires are presented in Sec.4.2.2. All measurements are based on the presented setups in Sec.3

4.1 Time of Flight Measurements

For the analysis of mixing on the scale of just a few atoms, ToF measurements are an ideal tool to identify the amount of different elements to appear inside a helium droplet. In the following a brief introduction to the mass spectroscopy of helium is given, however the main focus lies upon the measurement of helium with one dopant and helium with two dopants inside the beam.

4.1.1 Measurement of Helium Droplets

For further understanding of the ToF measurements, this section should highlight the properties of an undoped helium beam. As mentioned in Sec. 2.2 helium can undergo a phase transition to a superfluid state, depending on the stagnation pressure p_{st} and the temperature. When changing the pressure or the temperature of the nozzle, different droplet sizes are accessible. In a mass spectrum, the helium droplet beam appears as a series of peaks separated by the mass of one helium atom (4 amu). The temperature dependence of the signal is not intuitive and therefore shall be discussed here. At a temperature of 11 K and a $p_{st}=20$ bar more helium peaks are visible than at 9 K and $p_{st}=20$ bar, although at 9 K a greater amount of helium leaves the nozzle.

This phenomenon can be explained through the different droplet creation and the corresponding stability. For the ionisation of atoms, an electron beam with an acceleration

voltage of 89 kV is used. By reducing the temperature of the cold head, the helium droplet size distribution shifts to bigger droplet sizes. This leads to a wider distribution of helium signals, resulting in a lower intensity of all mass peaks. Therefore, for higher temperature (e.g. 12 K) the intensities of helium peaks are only distributed among few different mass peaks, which gives the circumstances that the detectable peaks are more significant. In comparison to 8 K, which relates to a higher mean droplet size (10^6 helium atoms), only miniature fragments of the droplets, which rarely occur, can be detected in the signal of the ToF. This process leads to a decrease of the helium peaks for small masses, although the amount of helium flow increases. This phenomena can be seen in Fig.4.1.

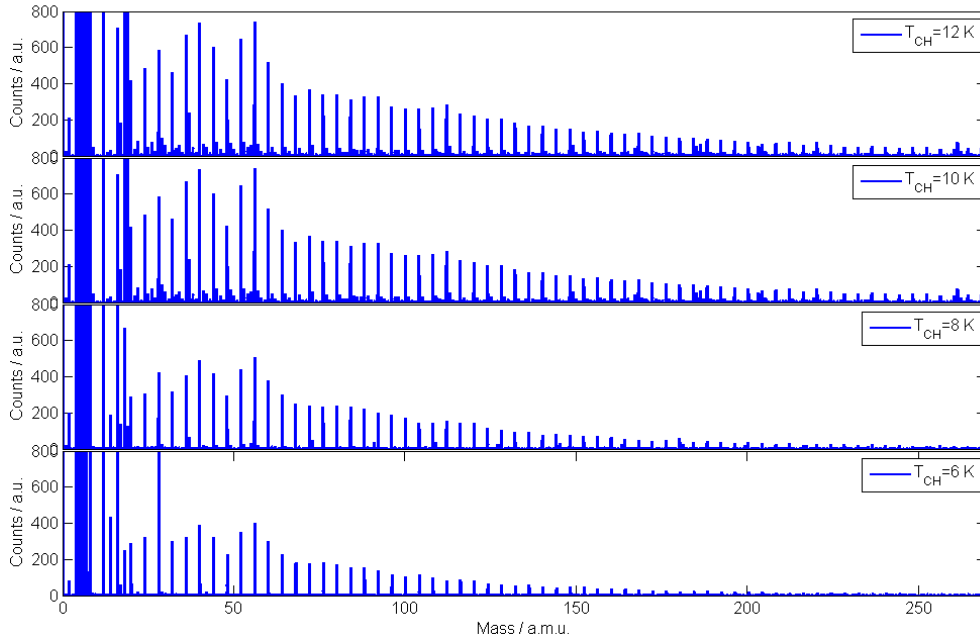


Figure 4.1: Helium spectra in dependence on different temperature of the cold head (T_{CH}) and with a constant p_{st} of 20 bar. The reduction of the helium signal for small masses, as described in the text, is visible. For masses of $m < 30$ amu, impurities in the vacuum are visible.

4.1.2 Monometalic Molecules inside Helium Beam

For helium droplets doped with pure elements, a significant change in the ToF spectrum can be observed. For small clusters with less than fifteen atoms, it is possible to distinguish the signal in dependence of the different isotopes. For higher number of atoms, the signal can be blurred because of overlapping signals from diverse cluster sizes. Additionally, the signal of the helium overlays the whole spectrum.

The doping of the clusters was done with a crossed beam setup, which was presented in Sec.3.2.1. To achieve the required partial pressure of the desired element within the pickup cell the temperature of the crucibles had to be adjusted. For the partial pressure of the examined elements, a minimum of 10^{-5} Pa has to be accomplished before it is even possible to detect the elements in the ToF.

Copper

For copper having only two different stable isotopes, it is possible to distinguish the spectrum for more than ten atoms per cluster. The isotopes of copper and their abundance are: ^{63}Cu with 69.17% and ^{65}Cu with 30.83%. For ToF measurements with copper, the peaks were measured with a cold head temperature of 9.5 K. In Fig.4.2 a spectrum is shown, for this spectrum conditions p_{st} of 20 bar and cold head temperature of 9.5 K were used. The oven temperature of copper was set to 1050 °C.

From Fig.4.2 some effects of a cluster with an atomic number below ten can be seen:

1. After every peak of a copper cluster, a small peak occurs, 18 amu heavier. These peaks are attributed to H_2O -groups within the vacuum. The resulting cluster ($Cu_n(H_2O)_1$) differs in weight by 18 amu, which is the mass of H_2O .
2. Mixing of the different isotopes leads to a change of the copper signal for different cluster sizes. Meaning that for Cu_1 , two peaks are measured, with the exact relation as the isotope abundance; for Cu_7 several peaks can be seen in Fig.4.2 (bottom). Following the random composition of each cluster, these peaks result of a mixing between the two different isotopes.
3. The reduction of the helium signal due to the copper signal is visible. Due to the evaporation cooling the helium signal detected by the ToF spectrometer is lower.
4. Even and odd oscillations of the clusters are visible in Fig.4.2. In comparison to even numbered clusters, the peaks for odd-numbered clusters were higher. These were already observed for different elements³¹. The origin of this intensity distribution of clustersizes is related to the ionisation energy needed for each cluster. Odd numbered clusters have a lower ionisation potential as even numbered clusters since the valence electrons of odd-numbered clusters are unpaired^{55 56}.

The last point mentioned above can be explained due to the electronic structure of copper ($[\text{Ar}] 3d^{10} 4s^1$). Copper has a fully filled 3d-orbital and one electron in the 4s-orbital, makes it a monovalent metal. Because of that, the conduction band of the solid can roughly be approximated as free-electron-like and the Fermi surface is nearly spherical. For a cluster of mono valent metallic atoms, the jellium approach had great success and even gives an explanation for the even odd oscillation of the presented spectrum

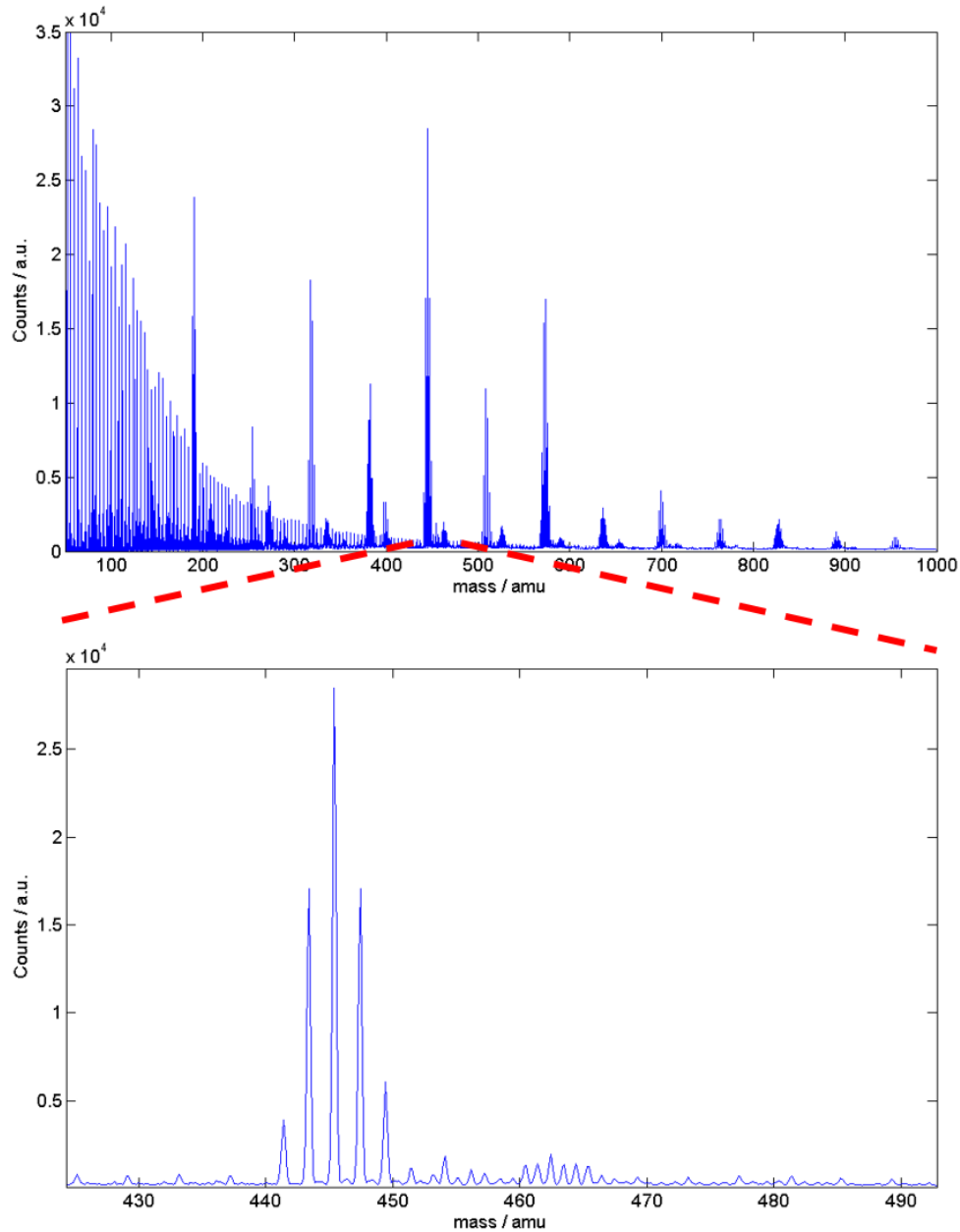


Figure 4.2: Top: ToF mass spectrum of copper doped helium beam. The cold head temperature was 9.5 K, the p_{st} was 20 bar and 1500000 sweeps were taken for this spectrum.

Bottom: The region marked with the red dashed line is magnified. The mixing of the two isotopes yields the measurement distribution. After the pure copper peaks, other peaks appear 18 amu heavier. These peaks can be assigned to an additional H_2O molecule on the copper cluster.

(Fig.4.2). A detailed theoretical explanation of the jellium model can be found in Ref. 57, whereas Ref. 56 gives an experimental comparison of different elements. Another detail in Fig.4.2 is the reduction of counts after the cluster size of nine. This drop in the detection for this kind of cluster is in good agreement with previous measurements made in sputtering setups. This behaviour can be qualitatively described in terms of a one electron shell model. In this model, the free electrons are assumed to be bound in a spherically symmetric potential well. This effect is well described by Ref. 58 and Ref. 59.

Gold

Having a similar electronic structure as copper, gold was also investigated in terms of ToF mass spectrometer analysis. Gold and copper are both elements of group 11 of the periodic system. The electron configuration for gold is $[\text{Xe}] 4f^{14}5d^{10}6s^1$. Having only one stable isotope ^{197}Au , gold is an ideal candidate to observe the even-odd oscillation. Having a slightly lower vapour pressure than copper, higher temperatures were necessary to achieve a reasonable signal in the TOF. This resulted in an oven temperature of $1100\text{ }^\circ\text{C}$. The cold head temperature was set to 9.5 K and p_{st} was set to 20 bar . The resulting ToF spectrum is visible in Fig.4.3.

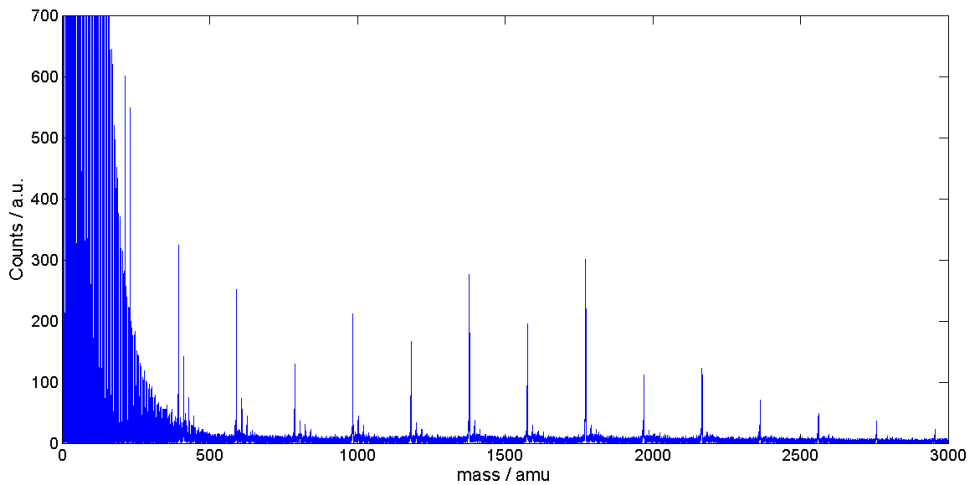


Figure 4.3: ToF mass spectrum of gold doped helium beam. The cold head temperature was 9.5 K , the p_{st} was 20 bar and 150000 sweeps were taken for this spectrum.

In the gold ToF spectrum, the even-odd oscillations appear. Additionally, the drop of counts after an atomic mass number of nine is very significant. As discussed previously, this drop of counts is due to the one electron shell model^{58,59}. At the mass numbers of 214 amu and 232 amu two peaks appear close to each other, whereas the peak for Au_1 T 197 amu is lower than the signal of He clusters. These two peaks can be assigned to

$Au_1(HO)_1$ (214 amu) and $Au_1(HO)_1 + H_2O$ (232 amu). It can be deduced from the spectrum, that single gold atoms are very common to attach to a OH molecule. In total, another peak would be expected, if another H_2O molecule was attached, at the mass of 250 amu. The absence of a peak at this position indicates, that only a maximum of $Au_1(HO)_1 + H_2O$ is attracted by one gold atom. Although a peak at 215 amu is also present, indicating $Au_1(H_2O)_1$, this peak is much less significant than the peak for $Au_1(HO)_1$.

This characteristic changes when looking to higher gold masses. At Au_2 peaks appear which are distinguishable from the helium signal. Additional three peaks, apart from the peak of Au_2 at 394 amu, appear. These peaks appear with a difference of 18 amu to the Au_2 peak and indicate as many as three H_2O molecules attached to Au_2 . Also, a very small peak is visible which indicates, that $Au_2(HO)_1$ at 411 amu is detected. From Au_1 to Au_2 the appearance of the additional HO changes totally. For Au_1 the additional HO peaks are higher than the original Au_1 mass. For higher gold cluster the OH peaks changes into H_2O peaks, with only a small contribution of OH peaks.

Nickel

Nickel has five different stable isotopes with the following abundance: ^{58}Ni with 68.077 %, ^{60}Ni with 26.233 %, ^{61}Ni with 1.14 %, ^{62}Ni with 3.634 %, ^{64}Ni with 0.926 %. For nickel the ToF spectra were taken at 9.5 K and p_{st} of 20 bar. To achieve the same partial pressure of nickel as for copper higher temperature are required, which required an oven temperature of 1380 ° C for the spectrum seen in Fig.4.4.

After the peaks of the nickel cluster, the same distribution appears but only 18 amu shifted to the right, which indicates H_2O molecules attached to the nickel cluster. The most important distinction between Fig.4.2 and Fig.4.4 is, that for nickel no even-odd oscillation can be observed. Different to copper, nickel has a completely different electronic structure ($[\text{Ar}] 3d^8 4s^2$). This results in a change of characteristic for the electronic structure and the assumptions for the Group 11 elements made above are not valid anymore.

The ionisation energy of small nickel clusters is shown in Fig.4.5. When comparing the ToF spectrum and the ionisation potential of nickel, the drop in terms of stability appears at an atomic number of seven. The drop at Ni_3 of Fig.4.5 can not be reproduced by the ToF spectrum. This may be the result of the overlaying distribution of different cluster sizes inside the helium droplet.

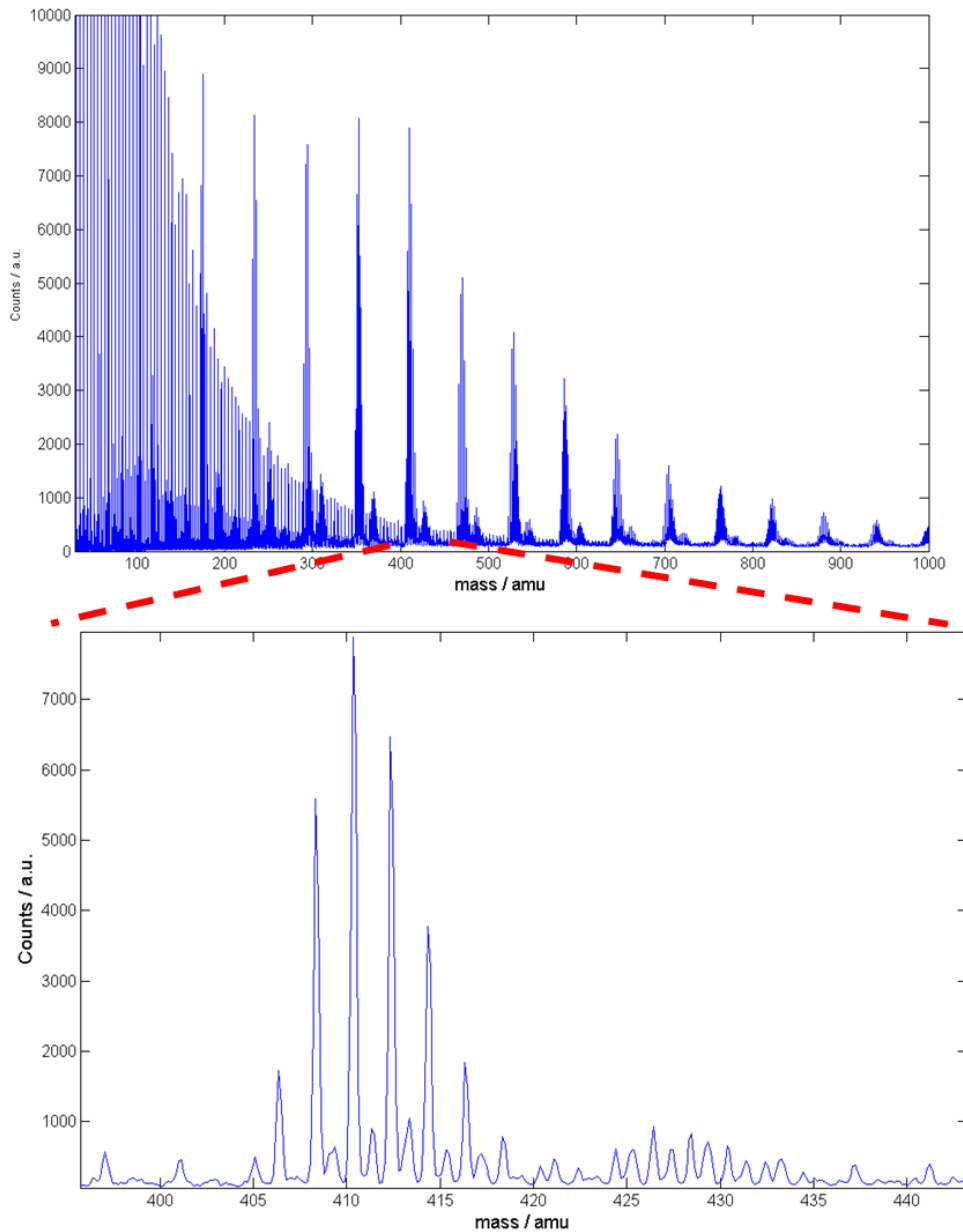


Figure 4.4: Top: ToF mass spectrum of a Ni doped helium beam. The cold head temperature was 9.5 K, the p_{st} was 20 bar and 1500000 sweeps were taken for this spectrum.

Bottom: The region marked with the red dashed line is magnified. The mixing of the five isotopes resulting in the measured distribution. After the pure nickel peaks, other peaks appear 18 amu heavier. These peaks can be assigned to an additional H_2O molecule on the nickel cluster.

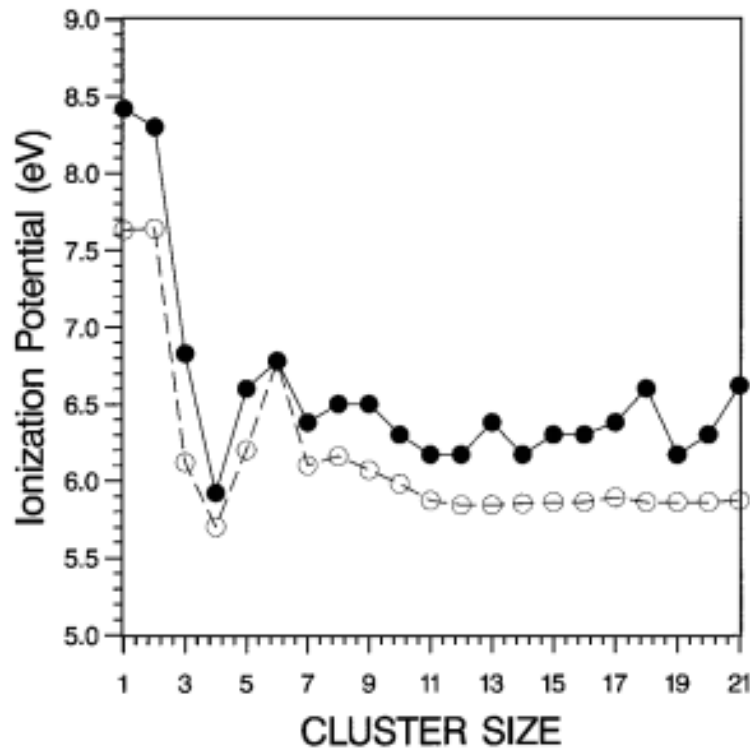


Figure 4.5: Ionisation potential in theory and praxis. Whereas the black circles indicate the measurement and the empty circles represent the theory. This figure is taken from Ref. 60.

4.1.3 Bimetallic Molecules inside Helium Droplets

In this section the ToF mass spectra of double doped helium droplets are presented. The cross beam set up enables to dope two different elements into the beam and to analyse the resulting signal in the ToF spectrometer. For this kind of measurement the intensity of the helium beam, measured by a Quadrupole mass spectrometer, has to be adjusted carefully. The binding energy released when forming a bond differs for each element. The released binding energy is the main source for attenuation of the helium beam. For nickel, the binding energy is 4,44 eV and for copper it is 3,49 eV. This leads to a weighted attenuation of the helium beam for each element. For the copper-nickel system, nickel has to reduce the helium current by 1.27 times more than copper to result in the same doping. The combination of Ni/Cu gained some interest in the last years for its potential to bind CO_2 molecules⁶¹.

The first spectrum of a helium beam doped with two elements was recorded for nickel being picked up first and copper second. First and second as seen by the droplet passing through the Pickup chamber. Before every experiment, a spectrum of each element for the same configuration as during the real experiment was recorded. This was crucial

to compare the influence of the mixing onto each element and the resulting peaks in the ToF spectrum. The configuration for this first spectrum at $p_{st} = 20$ bar and a cold head temperature of 9.5 K were used. The resulting spectrum is seen in Fig.4.6 Comparing the three spectra Fig.4.2, Fig.4.4 and Fig.4.6 it can be seen very clearly that

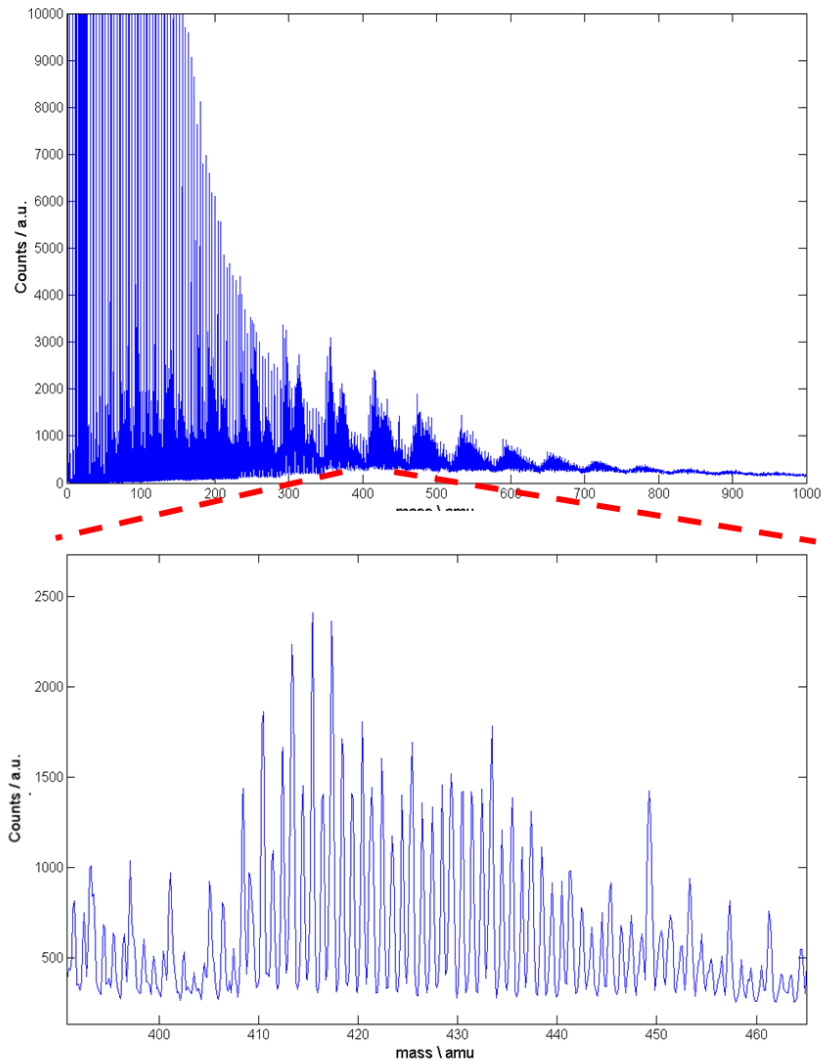


Figure 4.6: Top: ToF mass spectrum of nickel and copper doped helium beam. The cold head temperature was 9.5 K, $p_{st} = 20$ bar and 1500000 sweeps were taken for this spectrum. Here the nickel oven had a temperature of 1325 °C and the copper oven had a temperature of 950 °C.

Bottom: The region marked with the red dashed line is magnified. The mixing of the two isotopes resulting in a new form of the mass spectrum. New peaks in the spectrum appear leading to the conclusion, that new clusters of mixed origin are detected. For more details see the text.

new peaks appear. These peaks can only arise if nickel and copper mixed within the helium droplet. For both elements the mass numbers are very close together, so the peaks of the mixed elements arise between the single element peaks. The combination of the different isotopes of both elements leads to a signal which is smeared between the positions for the single elements. For the already shown spectra of the masses for seven atoms, the spectra are combined into a new plot to visualize the results as seen in Fig.4.7.

The spectra shown in Fig.4.7 (top and middle) have nearly the same counts for the

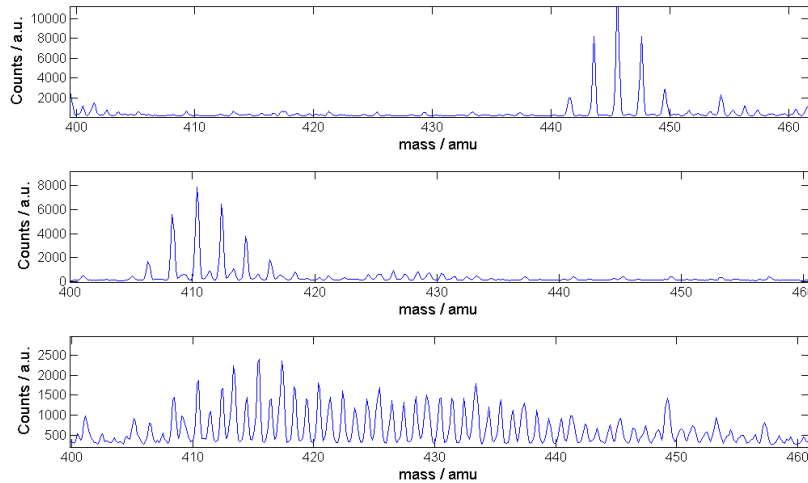


Figure 4.7: Top: ToF spectrum from copper recorded with 9.5 K and $p_s t = 20$ bar. For this spectrum, the oven temperature was set to 1050 °C.

Middle: ToF spectrum of nickel recorded with 9.5 K and $p_s t = 20$ bar. The oven temperature was 1380 °C.

Bottom: The combined signal for copper and nickel. For more information see text.

significant peaks. This distribution was desired, having roughly the same amount of counts for both elements. For nickel having more isotopes than copper, the distribution covers a larger mass interval, leading to lower count numbers for main peaks in this spectrum.

After closer analysis of the signal shown in Fig.4.7, it can be seen, that not all peaks appear uniformly. This is especially visible, by comparing the lines for pure elements before and after adding the other element. For copper most of the peaks completely vanish. The at first most significant peak at 445 amu disappeared completely, when comparing it to the nickel signal, where the significant peak at 410 amu is reduced but is still visible. From the absence of pure copper in this signal, it can be deduced, that copper prefers to make a bonding with nickel atoms rather than with other copper atoms.

This result can be explained by the different binding energy of the resulting cluster. For small clusters, the resulting formation and especially the cluster formation have been theoretically studied^{62 61}. Further analysis and discussion can be found in Sec.5.1.2

4.2 Temperature Dependent Analysis in a Transmission Electron Microscope

After analysing the alloying of a few atoms for the Cu/Ni system, a different size of alloying will now be approached. The next used elements are gold and nickel. This combination will be analysed because of the simple phase diagram (see Fig.2.4) making an investigation as simple as possible. The main goal was to create core-shell particles with a nickel core and a surrounding shell of gold. These particles were then analysed under a STEM while heating the sample. During the heating, a mixing of both elements was observed. For the analysis of the process, a novel technique was used.

Sample Preparation

The setup for this experiment is explained in Sec.3. The exact configuration will be discussed in this chapter. The first crucible was loaded with nickel and the second with gold. With this order of crucibles, the helium droplets were first doped with nickel atoms and afterwards with gold atoms. In this experiment, the helium droplets were doped with an approximately 30% Ni and 70 % Au atoms. Therefore the signal of ^4He was adjusted carefully. It was taken into account that the binding energies differ for both elements resulting in $\frac{E_{\text{BindNi}}}{E_{\text{BindAu}}} \approx 1.165$. Because of binding energy helium evaporates from the droplets and reduces the signal measured by the quadrupole mass spectrometer. With respect to the two different elements, the attenuation of the helium signal was set to be 30% of nickel and 60% of gold. The signal of the QMS changes for every cold head temperature.

During the measurement, a total of three different sizes of nanostructures should be created. Therefore the temperature of the cold head was sequentially changed from 8 K, to 6.7K and 5.4K. These temperatures relate to different sizes of cluster creation. For 8K clusters are created with nearly spherical shapes. At 6.7K the produced shape gets into an elongated form. For this size of droplets, the clusters synthesised inside start to arrange alongside the vortices. At 5.4K the resulting form of the clusters is wire shaped. The foreign atoms inside the droplets arrange alongside the vortices because of the tremendous size of the droplets these wire-shape nanostructures can become several 100 nm long.

In this experiment, a heatable TEM grid was used (see Fig.3.10) to control the temperature of the sample. The elements were heated up sequentially starting with nickel. The deposited mass was measured with the microbalance. For the deposition onto the TEM grid the parameters are listed here:

8 K: starting helium beam intensity $I_{4\text{He}}^0 = 9.8 \cdot 10^{-11} \text{A}$. At first the temperature of the nickel crucible was set to $T_{\text{Ni}} = 1080^\circ\text{C}$, resulting in a helium current of

$I_{He}^{Ni} = 7.95 \cdot 10^{-11} A$. Then the gold crucible was heated up to a temperature of $T_{Au} = 1230^\circ C$ resulting in a helium current of $I_{He}^{Ni+Au} = 3.8 \cdot 10^{-11} A$. With this configuration a deposition rate of $\dot{m} = 7 \cdot 10^{-5} \frac{\mu g}{cm^2 s}$ was achieved. For the deposition time onto the grid 50 s were chosen, resulting in total mass deposited for 8 K of $m_{8K} = 3.5 \cdot 10^{-3} \frac{\mu g}{cm^2}$.

6.7 K: the starting signal of helium was $I_{He}^0 = 1.36 \cdot 10^{-10} A$. The temperature of the nickel crucibles was adjusted to $T_{Ni} = 1050^\circ C$ resulting in a signal of $I_{He}^{Ni} = 1.075 \cdot 10^{-10} A$. Again after nickel, the gold crucible was heated to $T_{Au} = 1230^\circ C$, having a total helium signal of $I_{He}^{Ni+Au} = 5.3 \cdot 10^{-11} A$. The mass deposition rate was measured to be $\dot{m} = 7.3 \cdot 10^{-4} \frac{\mu g}{cm^2 s}$. 27 s were chosen as deposition time, resulting in a total mass deposited for 6.7 K of $m_{6.7K} = 2 \cdot 10^{-2} \frac{\mu g}{cm^2}$.

5.4 K: the starting signal of helium was $I_{He}^0 = 1.8 \cdot 10^{-9} A$. The temperature of the nickel crucibles was adjusted to $T_{Ni} = 1145^\circ C$ resulting in a signal of $I_{He}^{Ni} = 1.46 \cdot 10^{-9} A$. Again after nickel, the gold crucible was heated to $T_{Au} = 1400^\circ C$, having a total helium signal of $I_{He}^{Ni+Au} = 7 \cdot 10^{-10} A$. The mass deposition rate was measured to be $\dot{m} = 9.2 \cdot 10^{-4} \frac{\mu g}{cm^2 s}$. 2 s were chosen as deposition time, resulting in a total mass deposited for 5.4 K of $m_{5.4K} \approx 2 \cdot 10^{-3} \frac{\mu g}{cm^2}$.

The temperature values for the experiments for nickel have a big uncertainty. One would expect a value $\approx 20\%$ higher than the one measured. This uncertainty was due to an experimental error while starting the heating of the nickel crucible. The measured resistance of the crucible was 0.04Ω . For all measurements done before this experiment a resistance of 0.033Ω was measured, resulting in an error of at least 20% .

After deposition under UHV conditions, the samples were extracted from the main chamber by venting the chamber with dry nitrogen. After a short period of time under ambient condition, the samples were put under medium vacuum and were then directly transported to the STEM microscope. The exposure time to ambient condition was kept as short as possible to prevent contamination. FEI Titan3 G2 60-300 using the high angular annular dark field (HAADF) recording technique was used for further measurements. The heating curve of the specimen is shown in Fig.4.8.

4.2.1 Ni-Au Clusters

In this section nanostructures of the Au/Ni system with a diameter of below 10 nm are studied and their temperature behaviour is analysed. Nanoparticles forming a core-shell structure are of interest. These particles can be detected due to the lower atomic number of nickel, leading to a lower Z-contrast than gold.

Many particles with a core shell characteristic were visible on the substrate. In Fig.4.9 one example is presented. This particle has a spherical shape. Next to the cluster, a

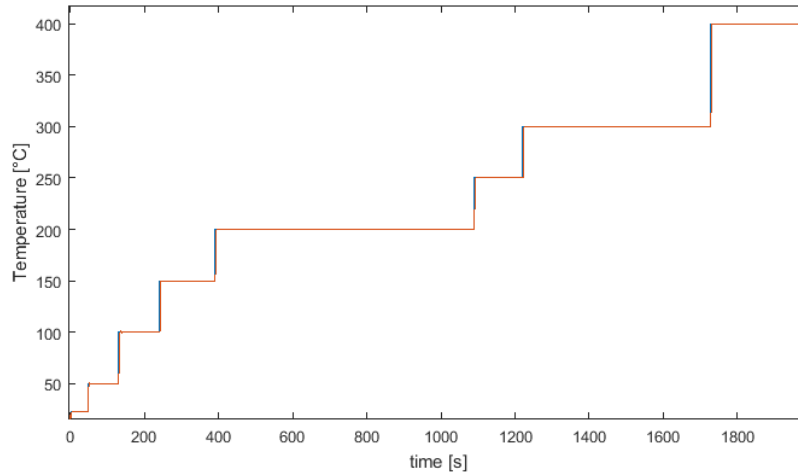


Figure 4.8: Time resolved heating curve of the Au/Ni specimen.

qualitative analytical investigation of the cluster is made. Two different methods were used: electron energy loss spectroscopy (EELS) and energy dispersive X-ray spectroscopy (EDX). The usage of these methods is motivated by the fact, that EDX is more accurate for elements with a high atomic number and EELS has a higher detection rate for elements with a low atomic number. In Fig.4.9 nickel counts are highlighted green and gold counts are highlighted red. To generate this element map for each pixel a whole spectrum of EDX and EELS was recorded. In these spectra, the specific energy of nickel and gold were selected and the intensity of each pixel displays how many counts were measured. This leads to a space resolved map in which the concentrations of the elements are mapped. This investigation supports the previous statement, that Ni has a lower atomic number and therefore the Ni core should be visible as a darker core of the particle.

Because atomic resolution is necessary for this study, only a small section of the TEM grid was observable. Therefore a region with three different sizes of clusters was chosen. For each of the clusters the relation of the diameter of the nickel core to the diameter of the gold shell is different. This is important because the dependency of different mass fractions is observable. Furthermore, two different crystal structures are visible among these three clusters. This leads to the unique possibility to observe directly diffusion of small clusters in dependence of the crystal structure. The region of interest for this experiment is presented in Fig.4.10.

The section of the specimen displayed in Fig.4.10 was observed during the heat up of the TEM grid. The starting temperature was set to 50 °C and the temperature increase was set in 50 °C steps. During the heat up also a temperature dependent position shift of the cluster was visible. This shift was due to temperature expansion of the heatable TEM grid. This shift required a refocusing of the TEM after every new temperature. Due

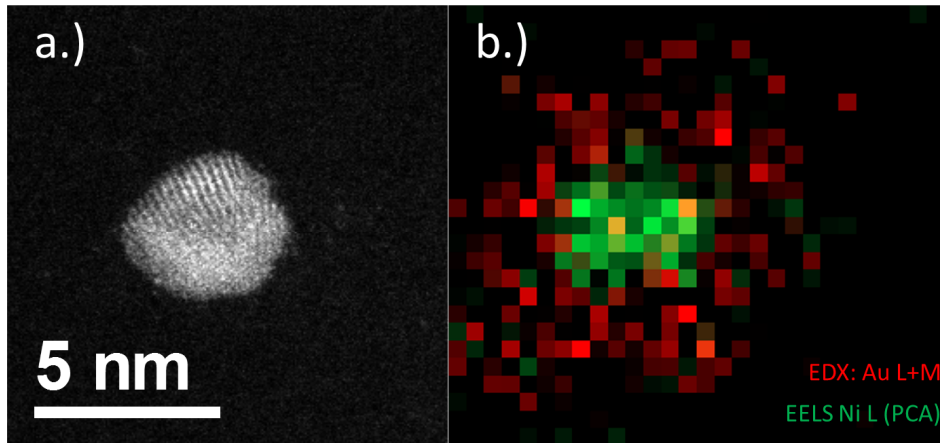


Figure 4.9: One cluster on Ni/Au.

Left: The darker region in the mid of the cluster indicates a nickel core surrounded by a gold shell.

right: An analysis of a qualitatively space resolved map of the cluster is shown. For this map, just the cluster was magnified more to analyse the cluster itself.

to the refocusing of the TEM the contrast configurations changed during the different temperatures.

Within this experiment, the three clusters were observed and the change with rising temperature was analysed. A sequence of pictures with the corresponding temperature is displayed in Fig.4.11. Here a very interesting phenomenon is visible: the nickel core of the bigger cluster vanishes before the nickel core of the smaller cluster on the left side vanishes. This is not intuitive, because it is common that smaller structures melt before the larger ones^{63 64}. This may be explained due to the more stable crystal structure of the small cluster being icosahedra. Also, other features were detected during the heat up:

- the cluster with an elliptical shape reduces its surface by forming a more spherical like shape,
- the biggest cluster loses its significant core at first, even before the smaller cluster with face centred crystal structure.
- the cluster with icosahedral structures has a stable core for $\approx 50^\circ\text{C}$ higher temperatures than the clusters with an fcc structure.

It seems that smaller clusters are more stable against higher temperatures than bigger structures. This conclusion is made based upon the results presented in this chapter.

Within this number of observations the alloying process is dependent on the diffusion of

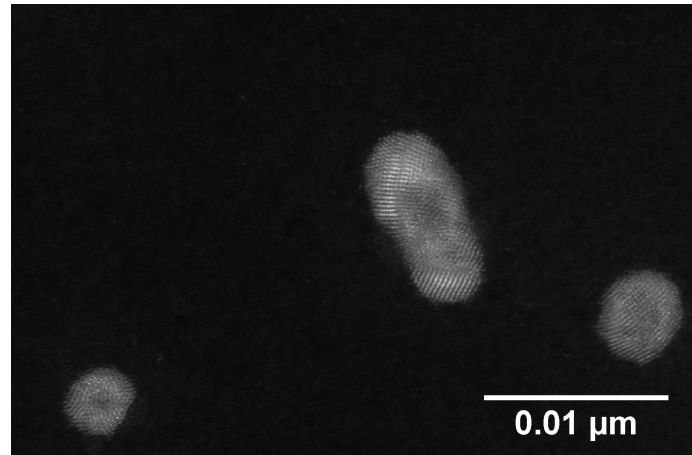


Figure 4.10: The region of interest for the Ni/Au experiment. Three different clusters with a visible Ni core are shown in the Figure. Here the cluster in the left corner has an Icosahedra crystal structure, whereas the two clusters on the right have a face-centered-cubic structure. This picture was taken at room temperature.

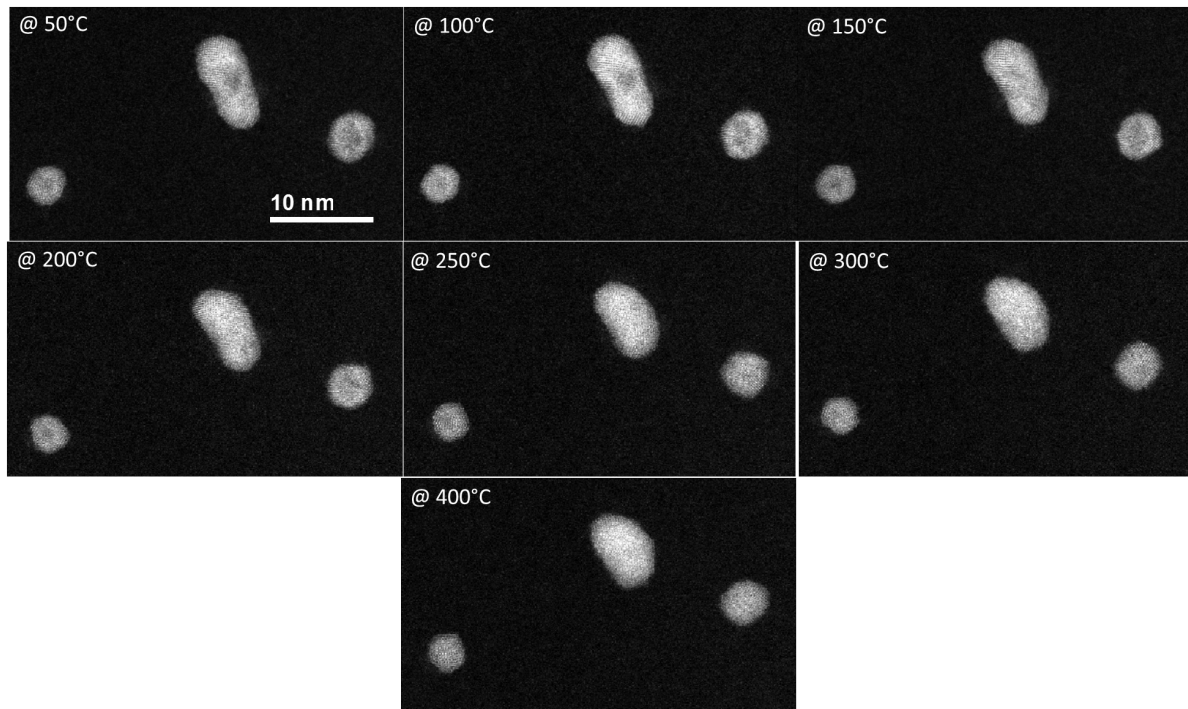


Figure 4.11: The region of interest from Fig.4.10 now is shown depending on different temperature steps. The interesting phenomenon is that the nickel core vanishes for different temperatures for each cluster.

one metal into the other one. This mechanism can be called counter diffusion⁴¹. This phenomenon is triggered through a change of position of two atoms on the interface

between the core and the shell. The changing of two atoms at the boundary between nickel and gold may have several different forms, when theoretical approached.

After the heat up of the sample to 400 °C the sample was cooled down to room temperature again. After cooling down within milliseconds the structure on the chip seemed to not have changed from the shape and structure they had at maximum temperature. This "freezing" of the atoms appears because the thermal energy of the atoms is reduced so fast, that a new arrangement is not possible.

4.2.2 Ni-Au Nanowire

During the preparation of the Ni/Au measurements the cold head had a temperature of 5.4K. This temperature gives rise to helium droplets in the range of μm diameter. Within this droplets, the resulting nanostructures building alongside the vortices have a elongated form. These new structures are often several hundred nanometres long. Although the time for deposition with 5.4 K cold head temperature onto the TEM grid was short, it was possible to locate several different core-shell nanowires. These wires have a nickel core and a gold shell. The shell does not completely surround the nickel core wire. These wires were analysed during heat up and several recordings of their temperature dependent changes were made. In Fig.4.12 one example of a core-shell nanowire is visible and the temperature dependent diffusion is shown.

The structure of the wire at room temperature has spots where the nickel core is

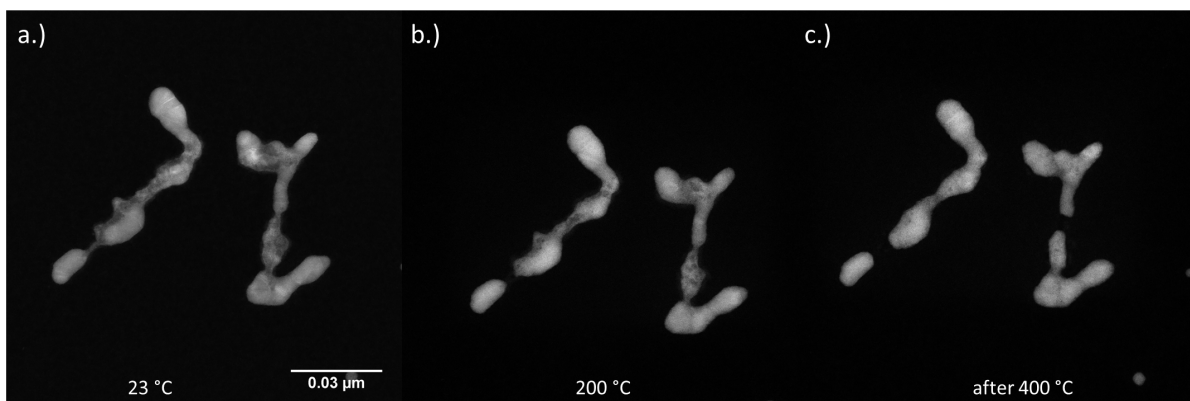


Figure 4.12: Picture of two Ni/Au nanowires with a nickel core and a not complete gold shell. For a.) the nanowires are at 23°C, the different contrast indicates the different elements. At b.) the mixing of both elements starts. The thermally induced diffusion results in a smoothing of the surfaces. c.) displays the nanowires after heat up. Mixing has taken place and the contrast over the whole structure is very homogeneous, leading to the conclusion that after 400 °C the elements have completely mixed.

visible. The gold surrounds the nickel core in cluster-like shapes alongside the wire axes. At a temperature of 200°C the mixing for the wire elements starts. When comparing the pictures at 200 °C and the wire after the heat up, much has changed. The wire broke on a spot where earlier a very thin nickel line had been. Also the shape of the nanostructures changes: the edges of the clusters get smoother and the complete form gets more compact. The small buckling of the wires retreat and disappear completely. All these effects can be explained due to temperature-induced surface diffusion. Due to the higher temperature, the mobility of the atoms at the surface rises leading to higher mobility. The structures of the nanowires result in a more spherical shape than before, meaning that the system reduces its surface.

Oxidation of Cluster

After the heating of the nanostructures different element specific measurements were performed. As mentioned above, before the heating all observed core-shell structures did have a nickel core and an outer shell of gold. The HAADF images taken from the clusters after heating did not show any material contrast, which was interpreted as total alloying of the clusters. When performing space resolved EELS and EDX measurements a new configuration of the clusters was found. The nickel diffused to the surface of the cluster. While performing EELS, the signal from oxygen overlaid the region where the nickel had been detected. The nickel diffused to the surface of the Ni/Au cluster seemed to have undergone an oxidation. When performing the same element specific measurements before the heating, the nickel oxide layer was not measured. In Fig.4.13 the different spatially resolved measurements are shown.

It is visible that the signal from nickel and oxygen covered the same regions. The gold core seemed nearly covered by the Ni/O layer. Previous studies have shown, that the shape of the nanostructures have roughly spherical shape on the TEM grid. With a spherical shape the interaction volume of the electrons from the TEM changes by travelling through the cluster. It seems that the main amount of the Ni/O signal is within the boundaries of the cluster. When Ni/O form a nearly closed shell, the interaction volume increases, especially on the boundaries of the cluster. This has been in agreement with the images of Fig.4.13 .

The starting configuration of these nanostructures was a nickel core and a gold shell, the EDX and EELS analysis revealed a switch off these positions. It seems that the gold core is not fully covered in the Ni/O layer. The effect of a separation of NiAu alloyed clusters to Au-core and NiO shell has been reported previously⁶⁵. A similar effect has been reported for just nickel clusters⁶⁶. Here the nickel cluster was irritated by an electron beam, which induced the growth of nickel oxide at the surface. Due to the electron beam, it was possible to show, that more and more nickel was oxidised, leading to a totally oxidised nickel cluster in the end. This phenomenon can be explained by

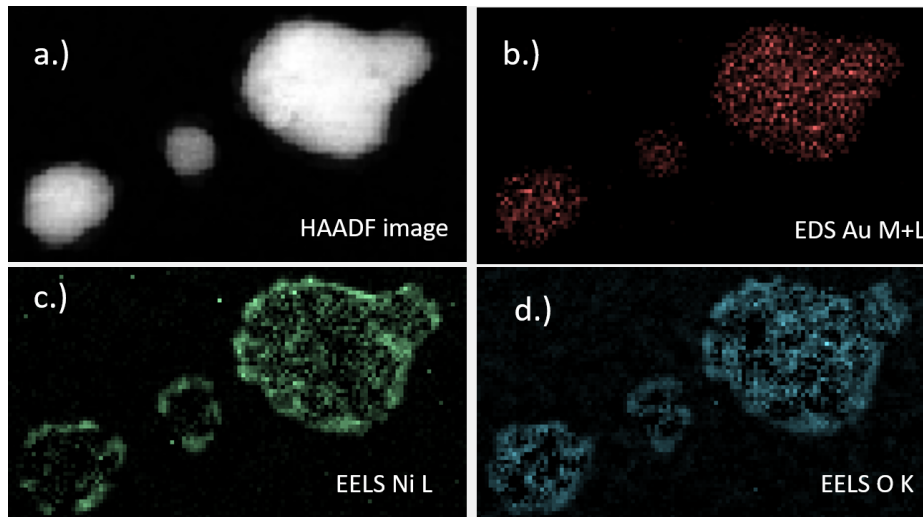


Figure 4.13: EELS and EDX spatially resolved measurement for Au/Ni clusters. In the upper left corner, the image of the nanostructures taken with HAADF is shown (a). The other three pictures are, respectively, two EELS images for nickel (c), oxygen (d) and one EDS spectrum for M+L shell transitions for gold in (b). When comparing the region marking nickel and oxygen, it is evident that both elements share the same spaces. The gold signal is located in the middle of the Ni/O signal. Before the heating, the cluster had a visible nickel core and no oxidation was observed.

the Cabrera-Mott kinetics⁶⁷. It seems reasonable that the same mechanism also appears at the clusters observed in this work. However, here not only the electron beam of the TEM was the cause, but also the high temperature of the specimen. A short explanation of the Cabrera-Mott kinetics will be given. When heating the specimen, the diffusion length of the nickel becomes large enough to travel to the surface of the cluster. On the surface an oxidation with one O atom is possible. After the first layers of NiO is build up, a negative charge builds relatively to the elemental nickel atoms. Due to the charge, more nickel atoms diffuse to the surface where the nickel oxide is. Due to this effect the nickel oxide diffuses to several regions on the gold cluster. This can be observed in the EELs and EDX images from Fig.4.13 well.

5 Computational Method

For some of the performed experiments, computational simulations were created to aid the analysis of the experimental data. Especially for the analysis of the ToF spectra and the alloying processes of small clusters, these simulations help to understand the effects behind these phenomena.

5.1 Time of Flight Measurement

In this section, the ToF spectra presented in Sec.4.1 are investigated in more detail, by employing simulations. Especially for mass spectra of clusters of two elements, the investigation with simulations brings new information about the mechanism of binding inside the helium droplets.

5.1.1 Mono Metallic Signal

For the measurements of the ToF spectra, one important parameter is the number of isotopes of each element. The signal for the same molecule can have multiple peaks due to different masses of the involved isotopes. To handle this kind of problem for single element doping the spectrum of the ToF signal was reconstructed. This was possible as each metal cluster is hypergeometrically distributed:

$$h(k|N; M; n) := P(X = k) = \frac{\binom{M}{k} \cdot \binom{N-M}{n-k}}{\binom{N}{n}} \quad (5.1)$$

with N being the total number of counts for one element, M the number of counts for one isotope, n is the number of draws and k is the number of observed successes for one isotope. Here $h(k|N; M; n)$ represents the probability of acquiring k specific isotopes, when detecting n atoms.

The program creates a new contribution for each element. With a random number, an isotope is chosen, resembling their distribution. For clusters with a mass higher than one atom, more random numbers are generated. These new random numbers are used to choose again isotopes, resulting in the possibility to simulate higher mass peaks of the ToF signal. Implying a specific number of repetitions the code recreates the ToF spectra for mono metallic clusters. The comparison of the simulation and the measured

ToF spectrum can be seen in Fig.5.1. For the first simulation, only peaks related to pure metal molecules are taken into account. At high masses (405 amu to 430 amu), the helium signal (multiple of 4 amu) is small compared to the peaks from the nickel cluster. Therefore accounting for the signal from single attached helium atom in this region of simulation is not necessary. The result of the simulation resembles the measurement very well.

On the right side of the spectrum, small peaks occur, which are not displayed in the simulation. These peaks are too intense to be declared as noise. These peaks occur, as previously discussed, because H_2O molecules can attach to Ni_7 molecules. When performing magnification of the noisy signal (from 424 amu to 436 amu) the same distributions as for Ni_7 appears again. This confirms that these peaks, are signals of Ni clusters plus one H_2O . The peaks that are predicted between 425 amu and 430 amu by the simulation are small in comparison to the signal of the monomolecular water.

5.1.2 Bimetallic ToF Signal

For the spectra of bimetallic clusters, the computational analysis has tremendous advantages. It is possible to investigate the signal and to analyse the probability that specific clusters are formed. With this technique, it is possible to predict the resulting proportions of mass peaks for specific cluster sizes, formed by nickel and copper. The results are used to understand the very nature of binding of a few atoms and to predict compositions at specific masses.

The structure of the program described above, makes the addition of a new element simple. The number of stable isotopes of both elements are summed up. In Fig.5.2 one can see a bimetallic cluster with 7 atoms. The distribution arises from both Ni and Cu isotopes. For the deep blue bars the possibility for a nickel atom to appear was set to zero. For the lighter blue, the possibility for an appearing nickel rose to $\frac{1}{7}$, whereas the probability for copper had been reduced by $\frac{1}{7}$. Continuing until the possibility for nickel rose to 1 and for copper to 0 the bars are added together and the resulting spectra can be seen in Fig.5.2(bottom).

Apart from one pure Cu peak at the right end of the spectrum no other mono metallic Cu peaks were measured, but rather a mixture of Ni and Cu, which can be seen in Fig.5.2. It seems that for Ni-Cu cluster with seven atoms the ones with a larger number of Ni atoms are measured more frequent. The difference of the simulation to the measurement in fig.5.2 is significant. In addition, a background He signal is visible (mass 4 amu) within the measurement, which is not considered in the simulation. The results shown in Fig.5.2 follow the theoretical results of a DFT calculation for small cluster in two dimension from Ref. 62. In the calculation, the energy for pure nickel clusters is higher than for Ni-Cu-mixed clusters. In contrast to the lack of counts for pure copper clusters in the mass spectra, Derosa *et. al* further calculated a reduction of energy for an increasing amount

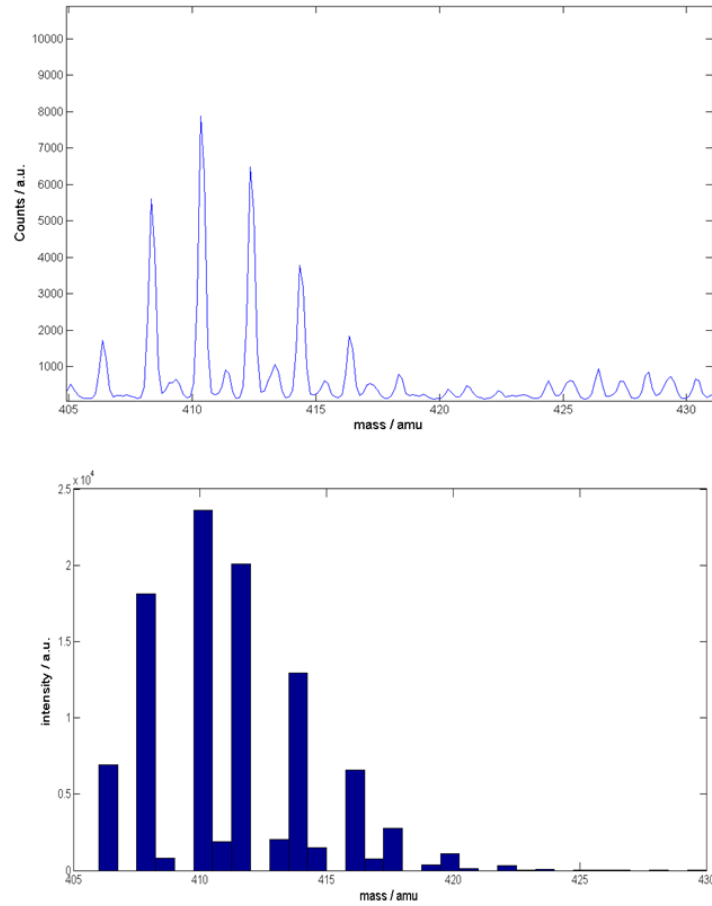


Figure 5.1: The simulation of the ToF signal and the measurements for the mass numbers related to Ni_7 are presented. The simulation (bottom) can reproduce the mass spectrum rather well. The significant peaks of the spectrum have the same relative height and same position in the simulation as in the measurement.

of copper atoms in the clusters. This would lead to an increase in the counts for pure copper cluster, which is not visible in the ToF spectra. Important to mention is that the calculations performed by Derosa *et. al* are for Ni/Cu systems, with a restriction to clusters with five atoms. The lack of counts for pure copper clusters with five atoms is visible in Fig.5.2. This interval is enhanced displayed in Sec.7.

As mentioned before the simulated signal in Fig.5.2 does not match the measured ToF mass spectra. To obtain a better fit, the simulation is extended by accounting for the helium signal. The intensities in the simulation were modified, because not all fractions of Ni and Cu appear equally. The previous measurements were taken into account, therefore the intensities for pure element clusters were reduced and the intensity for

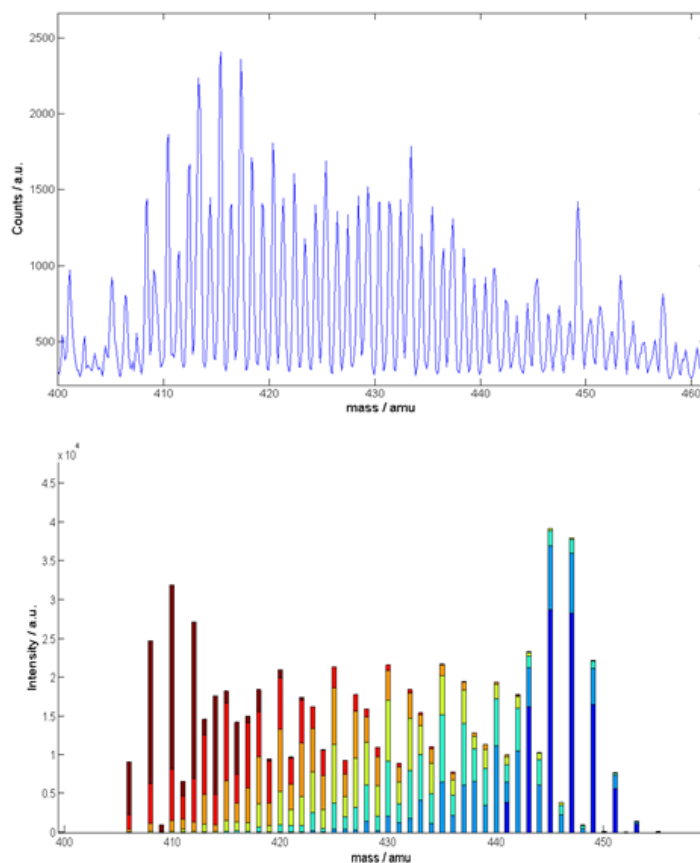


Figure 5.2: The comparison of the theoretical predicted and the measured ToF spectrum for a cluster of seven atoms. Here the difference in the shape of the two curves is significant. The colour of the bar graphs marks the portion of the signal starting from red, just nickel, to blue just copper.

a cluster with a high fraction of nickel was enhanced. This transformation resulted in the following fit for the ToF spectra seen in Fig.5.3. The simulation presented in Fig.5.3(bottom) reproduces the signal from the measured spectrum well. The resolution in the histogram plot is reduced by binning widths of one amu to provide a smooth spectral shape.

The investigation of mass spectra for helium droplets, doped with two different elements, shows that not every configuration appears with the same probability^{68 13}. The predicted results of previously done DFT simulations for clusters containing Ni-Cu atoms, were not reproduced⁶² as we observe a smaller amount of Cu_N clusters. The simulated molecules from Ref. 62 are highly likely to have a different molecular structure.

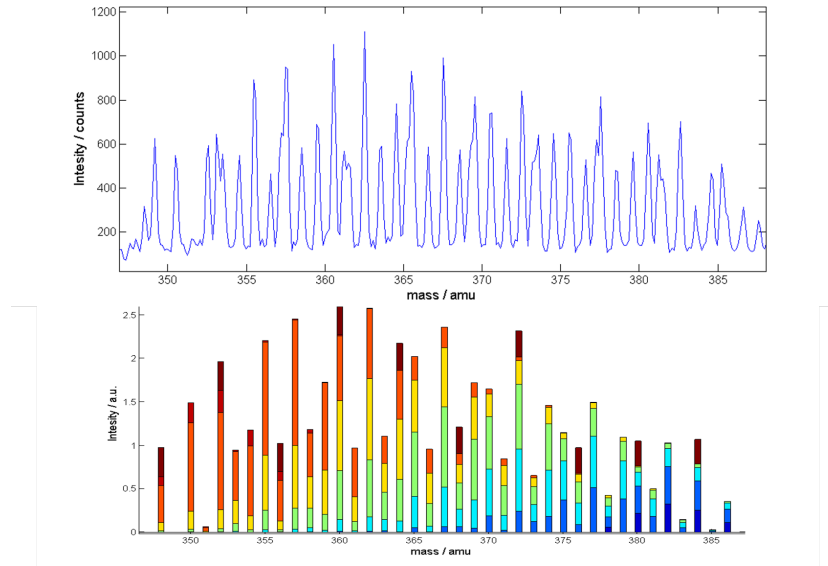


Figure 5.3: Top: Here the ToF spectrum for a copper temperature of 1000°C and nickel 1400°C is displayed

Bottom: The simulation of the ToF spectra with weighted abundances for different compositions. In particular, the intensities for the pure elements were reduced by a factor of 10. The colouring schemes are the same as in Fig.5.2. Additionally, in dark red, the helium signal was added.

5.2 Diffusion in Au/Ni core shell structures

In this section, the HAADF images from Sec.4.2.1 are further analysed. In particular the diffusion of Ni and Au is investigated and the temperature dependence of the diffusion length is extracted from the images.

5.2.1 Principle

For the diffusion process of Ni-Au core-shell particles, the different Z-contrast for gold and nickel indicates the region where the concentration of each element is high. As gold has a much higher Z contrast than nickel, the main part of the measured signal stems from the Au shell. At room temperature both core and shell are clearly separated but can intermix when exposed to higher temperature. When intermixing is achieved the observed intensity distribution is similar to a intensity profile of the spherical monometallic cluster. When performing a horizontal cut through the centre of the cluster, an intensity profile can be recorded as a function of the cluster's temperature. This profile can be used to identify the degree of intermixing. In HAADF images with sub-atomic resolution, the single atomic layers would disturb the homogeneous profile of the cluster.

To overcome this problem, the profile was acquired over a rectangular shape. Here the smaller axis includes more than three atomic layers to smoothen the resulting radial density. The area of the shape is averaged, alongside the shorter flank, resulting in a 2-dimensional density profile. The resulting signal represented the mean signal over the cluster. To eliminate the errors due to thermal expansion of the TEM grid, the images were centered around the cluster. This procedure is shown in Fig.5.4 for the smallest cluster of Fig.4.10.

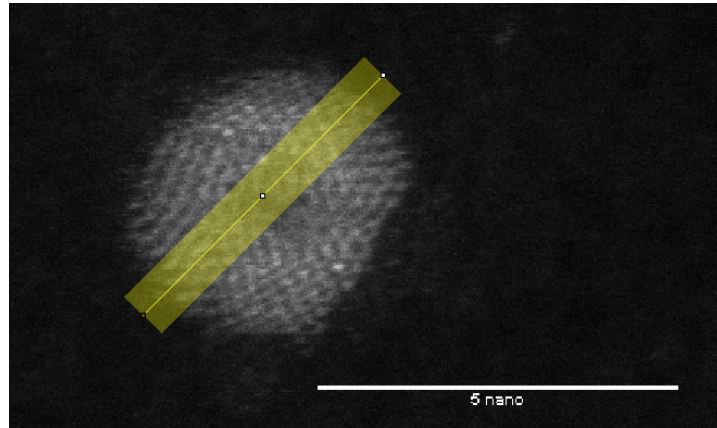


Figure 5.4: The procedure discussed above is shown in this image. The darker region in the centre is due to the Ni core, which has a very low Z-contrast. A rectangular shape is put over the HAADF image of the cluster at 23°C. Along the short flank of the shape, the signal is averaged, resulting in a density profile for this cluster shown in Fig.5.5

With this method, a radial intensity profile of the smallest cluster from Fig.4.10 was recorded. The shape of the cluster in Fig.5.4 is spherical. This shape indicates, that the cluster will not change its shape during the heating process, making it ideal for recording an intensity profile at different temperatures. To reduce the signal of the grid, the intensity of the background ($I_{background}$) was subtracted from the signal. Further, the signal was divided by the sum over all intensities. This had to be done, because after several heating steps the TEM had to be refocused. When refocused, the inner routines of the imaging software changed the settings for contrast, brightness etc.. Assuming that the total number of the atoms stays the same, the resulting profile can be modelled as:

$$I_{result} = \frac{I_{measured} - I_{background}}{\sum_{n=0}^N I_n}, \quad (5.2)$$

for N being the number of pixel of the recorded rectangular shape. An example of the intensity profile at three different temperatures can be seen in Fig.5.5. In the central region of the profile, an intensity minimum is observed for 50°C and 200°C. This minimum

results from the lower contrast of the Ni core inside the cluster. During heating, the density profile changes. The development in the profile shape indicates the diffusion of the elements. At 400°C the shape of the profile did not have a local minimum anymore. The boundary of the nickel core to the gold shell was clearly visible at room temperature, but disappeared for higher temperatures. This leads to the conclusion, that the nickel core diffused into the gold and vice versa.

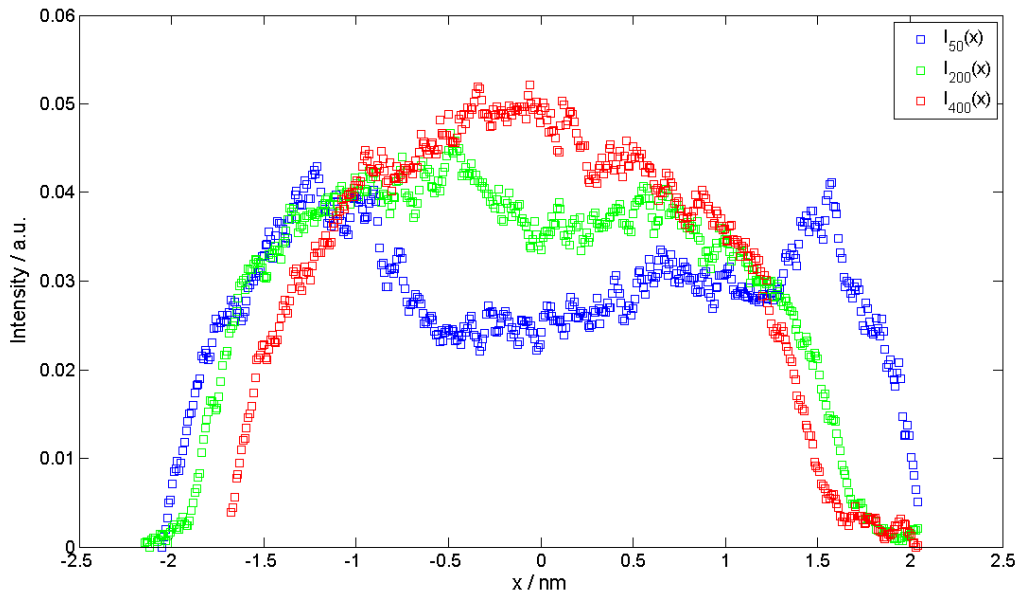


Figure 5.5: The intensity profile of a heated cluster at 50°C, 200°C and at 400°C. The change in the centre of the cluster is visible.

With this procedure, the temperature dependence of the diffusion length of gold and nickel can be investigated. Nickel, due its much lower nuclear charge contributes nearly no additional contrast in an HAADF image in comparison to gold. It is important to mention that the gold shell was capable of passivating the nickel core, as no oxidation was observed before the heating. When nickel nanostructures are observed in the TEM without a passivating layer a severe oxide layer has formed⁶⁹. The initial configuration of the cluster can be seen in Fig.4.9 with a nickel core and a gold shell.

Theoretical Principle

As previously discussed, the intensity profile $I(x, t)$ changes as function of the substrate temperature. Jones *et.al*⁷⁰ and LeBeau *et.al*⁷¹ have shown, that the measured HAADF intensity is linearly dependent on the thickness of the observed structure. In addition, different elements contribute more or less to the total intensity due to their atomic charge

Z . As a result, the measured intensity I_{meas} is proportional to the sample's thickness $l_{tot}(x)$. For a spherical cluster containing two elements the l_{tot} can be easily described as:

$$l_{tot}(x) = 2 \cdot \left(\rho_{Au} \left(\sqrt[2]{r_{Au}^2 - x^2} - \sqrt[2]{r_{Ni}^2 - x^2} \right) + \rho_{Ni} \sqrt[2]{r_{Ni}^2 - x^2} \Theta(r_{Ni} - |x|) \right), x \in [-r_{Au}, r_{Au}] \quad (5.3)$$

where r_{Au} is the radius of the gold shell, r_{Ni} is the radius of the nickel core, with ρ_{Ni} and ρ_{Au} being the nickel and gold element specific Z -contrast. A Heaviside step function Θ was used to model both the Ni core and the Au shell. To treat the diffusion of the

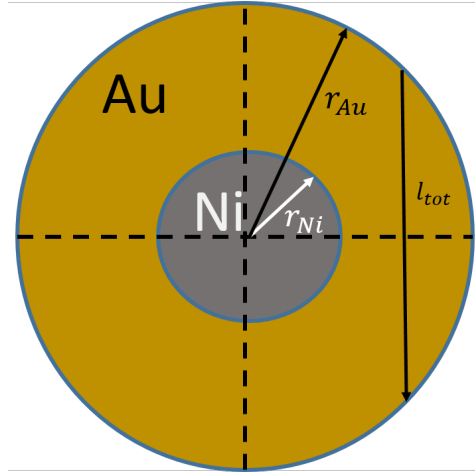


Figure 5.6: In this picture a 2-dimensional cut through a core-shell cluster is made. Here the difference radii of the elements are marked and also the l_{tot}

Ni/Au system the well known time dependent diffusion equation has to be solved:

$$\frac{\partial^2 u(x, t)}{\partial x^2} - \frac{1}{D} \frac{\partial u(x, t)}{\partial t} = 0. \quad (5.4)$$

Here $u(x, t)$ is the intensity profile of the cluster and D is the diffusion coefficient. This equation describes the diffusion of gold into nickel. For solving Eq.5.4 the initial value problem $u(x, 0) = f(x)$ has to be solved. Starting with a configuration of two separate species (as seen in Fig.5.6) $f(x)$ can be constructed:

$$f(x) = u_{Ni}(x, 0) + u_{Au}(x, 0) \propto l_{tot}(x) \quad (5.5)$$

with $f(x)$ is the intensity profile of the cluster at $t = 0$. $f(x)$ is the shape dependent function, describing the intensity alongside a radial cut through a cluster. As ρ_{Ni} is much smaller than ρ_{Au} , the observed change in the intensity profiles is mainly due to position changes of gold atoms. It is therefore possible that the contribution from nickel is set to zero and only gold diffusion is simulated. This leads to a simple form of the one

dimensional diffusion equation for gold.

One basic routine for solving Eq.5.4 is the well know approach based on the Fourier transformation of $u(x, t)$. This approach can be found in textbooks⁷² and therefore will not be discussed here in great detail. Eq.5.4 is solved in Fourier space with the following form:

$$\hat{u}(\theta, t) = \hat{f}(\theta)e^{-D\theta^2 t} \quad (5.6)$$

where θ corresponds to the inverse length in the Fourier space. If we transform this solution into real space, the following convolution integral is obtained:

$$u(x, t) = \int_{-\infty}^{\infty} f(y) \frac{1}{2\sqrt{\pi Dt}} e^{-\frac{(x-y)^2}{4Dt}} dy. \quad (5.7)$$

It is clearly visible that $u(x, t)$ is a function of the product Dt . Note that the diffusion coefficient D changes with increasing temperature T . The form $D(T) \cdot t$ reveals the underlying mechanism of diffusion, namely that either progressing time or increasing temperature can initiate the migration process. As a result we can write $u(x, t)$ to $\tilde{u}(x, D(T)t) = \tilde{u}(x, \chi)$ with $\chi = \chi(t, T)$ and use χ as fitting parameter to reproduce the measured intensity profiles. The resulting intensity can be recorded as an overlap of the Ni-signal and the Au-signal in the following form:

$$I(x, \chi) = I_{\text{Ni}}h_{\text{Ni}}(x, \chi) + I_{\text{Au}}h_{\text{Au}}(x, \chi) \quad (5.8)$$

where the height of the layer $h_i(x, \chi)$ can be directly linked to the radial intensity $u(x, \chi)$. In Fig.5.7 the comparison between the measured profiles and the solution of Eq.5.4. is presented.

To model the alloying process a fit is made for each recorded temperature dependent radial intensity profile. The diffusion length of the Ni-Au system is then determined by fitting each intensity profile, to give an estimation of how far the diffusion has already progressed. This system can be modelled by starting from the initial configuration of Eq.5.5 and solving the time-dependent diffusion equation for the radial intensity profile. The various measured intensity profiles are then fitted to the diffusion profiles, with the fitting constant χ , which determines how far the diffusion process has progressed. Each measured intensity profile $I(x, \chi)$ corresponds to a profile $u(x, \chi)$. From the intensity profile, the temperature dependence of the diffusion length can be determined. The diffusion length is defined to be the length x_{Diff} , where $u(x_{\text{Diff}}, \chi) = \frac{1}{e}u(x < r_{\text{Ni}}, \chi)$.

When investigating the diffusion length, a dependence of $I \approx \exp(-\beta/T)$ for the temperature was found. The diffusion lengths for different temperature are plotted in Fig.5.8. Here a significant rise of the diffusion length exceeding the particle size is observed for temperatures above 300°C. This is related to the vanishing contrast of the nickel core. At this temperature, a total alloying of Au and Ni is observed.

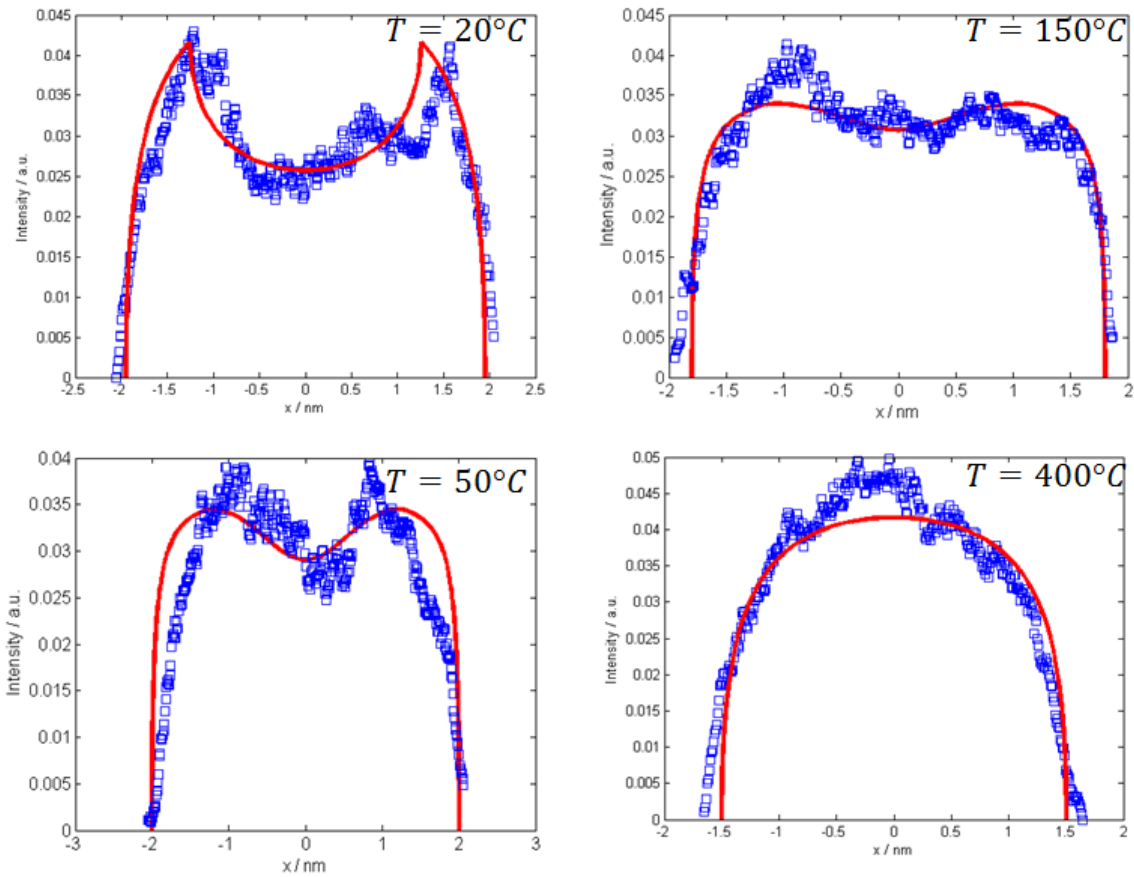


Figure 5.7: Fit for the observed intensity profiles using Eq.5.5 and Eq.5.8. The starting configuration $f(x)$ is well described by assuming two completely separated elements inside the cluster. When the heating of the specimen starts the diffusion process is enhanced resulting in a flattened profile. Note here the y-axes displays the results as defined in Eq.5.2.

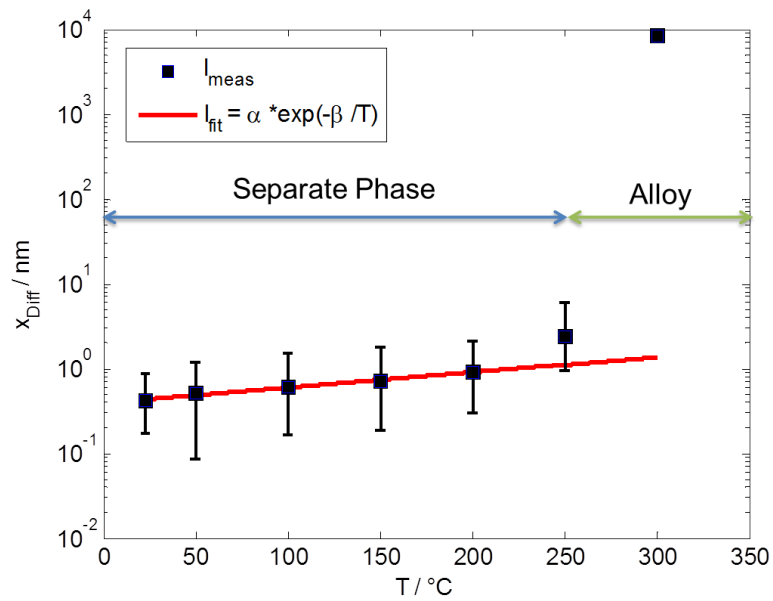


Figure 5.8: The temperature dependence of the diffusion length of a Au shell into a Ni core. The diffusion length is determined by a fit of intensity profiles taken from HAADF images of a cluster to density profiles taken from Eq.5.8. It is possible to determine the specific diffusion length for every temperature. When the diffusion length exceeds the particle size by orders of magnitude a complete intermixing is achieved.

6 Conclusion

In this thesis, time of flight spectra of doped helium droplets are analysed. The helium droplets were doped with three different elements and their spectra were discussed. For gold and copper, even-odd oscillations in cluster sizes below ten atoms per cluster could be identified. For nickel also mass spectra within helium droplets were presented. Closed electron shells were observed in clusters with more than nine atoms.

Bimetallic clusters from nickel and copper in helium droplets were synthesised and mass spectroscopically measured. The differences between the single atom spectra and the mixed spectra were investigated. A simulation method was developed to reconstruct and analyse the recorded spectra. Additionally, the portions of nickel and copper in mixed clusters in mass spectra could be determined, showing a tendency for the formation of nickel rich clusters. Especially low intensities for pure copper cluster were obtained.

Ni-Au core-shell clusters in a wide size range were created within the helium droplets and used for temperature dependent transmission electron microscopy studies. Core-shell nanowires and core-shell clusters were detected on the grid. Within these studies the temperature dependent alloying process of gold and nickel at nanoscale was observed up to a temperature of 400°C. A mixing was determined in the temperature region above 300 ° C. Also the temperature dependency of the diffusion length was determined by using a special simulation process. In this simulation, the HAADF profile of the core-shell clusters were used to create a radial density profile. This was possible due to the high Z-contrast of gold and in comparison the very low contrast for nickel. This profile was then fitted by a solution of the diffusion equation. With the change of the profiles of the clusters it was possible to determine the change in diffusion length for every recorded image and temperature.

The oxidation of the core-shell clusters of Au-Ni was observed after the heat up by spatially resolved element specific EELS and EDX. Due to the gold shell, it was possible to prevent the nickel from oxidation. The starting configuration of nickel as core element and gold as shell element seemed to switch during the heat up. EELS and EDX spectra were used to identify a shell of nickel outside the cluster. Furthermore, the signal of oxygen seemed to cover the same region as nickel. The images indicated a nickel oxide layer at the outside of gold core which was not completely covered. This process can be explained by the Cabrera-Mott model, in which the first appearing nickel oxide layer on the surface of the cluster supports the diffusion of more nickel to the surface.

7 Appendix

7.1 Absorption Spectra of Cluster

As mentioned in Chapter.3 the measurement procedure and the results for absorption spectra for the cluster on fused silica are presented here. The aim of these measurements was to detect surface plasmon resonances (SPR) near the visible light regime. Therefore clusters of gold and silver were deposited onto fused silica. Both materials are known to have surface plasmon resonances in the visible light spectrum^{73 74}.

For all measurements performed, a significant coverage of the substrate was necessary. Due to the rather limited flux of helium droplets, all experiments required hours, in which the fused silica was exposed to the helium beam doped with the desired element.

Silver

For silver, the properties to create nanostructures were adjusted. In detail, a cold head temperature of 5.4 K was used, the silver was heated to $\approx 950^\circ \text{C}$ and p_{st} was at 20 bar. With this configuration and strong silver doping the helium beam intensity was reduced by a factor of 75 %, resulting in a mass deposition rate of $3 \cdot 10^{-5} \frac{\mu\text{g}}{\text{cm}^2 \cdot \text{s}}$. The fused silica was then exposed to the helium beam for 2 h. After the deposition the mass deposition rate was measured, which stayed constant.

Afterwards, the fused silica was taken out of the measurement chamber and was immediately carried to the UV-spectrometer where an absorption spectrum (Fig.7.1) was recorded.

Fig.7.1 shows absorption in two regions from 900 nm to 700 nm and from 400 nm and 600 nm. The peaks from 900 nm to 700 nm appears also for clean fused silica specimen and therefore can be assigned to the spectrograph itself.

When comparing the absorption spectra of silver with results of Ref. 75 the results seem to fit very well for nanoparticles with a diameter of 36 nm.

Gold

For gold structures, a cold head temperature of 6.7 K and p_{st} 20 bar were applied. The gold oven was set to a temperature of 1240° resulting in a decrease of the helium beam

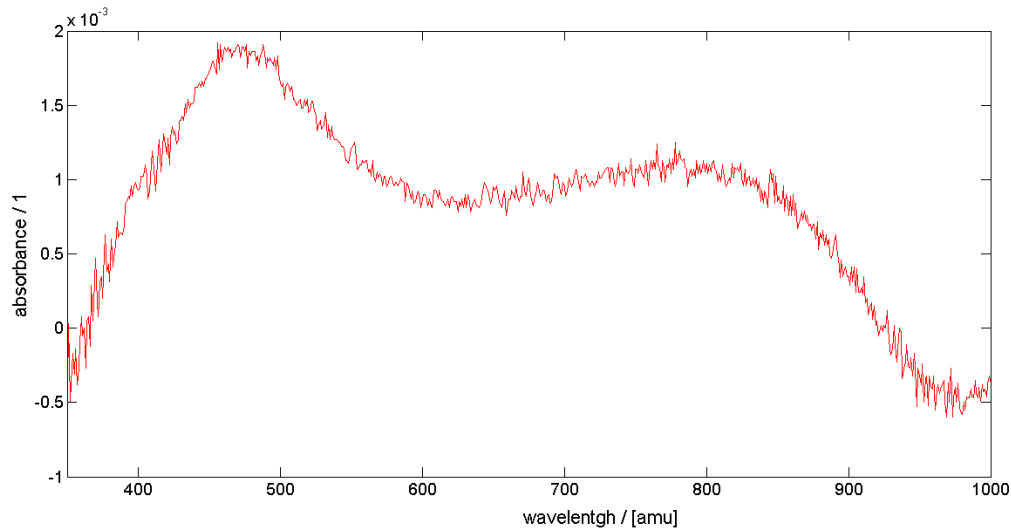


Figure 7.1: Absorption spectrum of silver nanowires deposited onto a fused silica plate. Here the absorption peak for silver is between 400 nm and 600 nm.

intensity of 60% and a mass deposition rate of $5 \cdot 10^{-5} \frac{\mu g}{cm^2 s}$. With this configuration the fused silica was exposed to the doped helium beam for 3 h. With this configuration, Fig.7.2 was measured. After the measurement time the deposition rate seemed to have dropped from $5 \cdot 10^{-5} \frac{\mu g}{cm^2 s}$ to $3 \cdot 10^{-5} \frac{\mu g}{cm^2 s}$. Additionally, the signal of the helium beam current seemed to have dropped. This seemed to be a long-time effect for the helium source. In Fig.7.2 the absorption of gold clusters in the visible light is illustrated. The peak between 500 nm and 700 nm can be compared to different other results of SPR profile for gold cluster⁷³. The drop in deposition rate indicated, that different sizes of clusters were deposited. Also in this spectrum, a small peak after 900 nm coming from the fused silica, can be identified, as seen previously for the silver spectrum.

The SPR seem a useful and fast analysis tool to investigate the size distribution of different clusters when deposited onto fused silica.

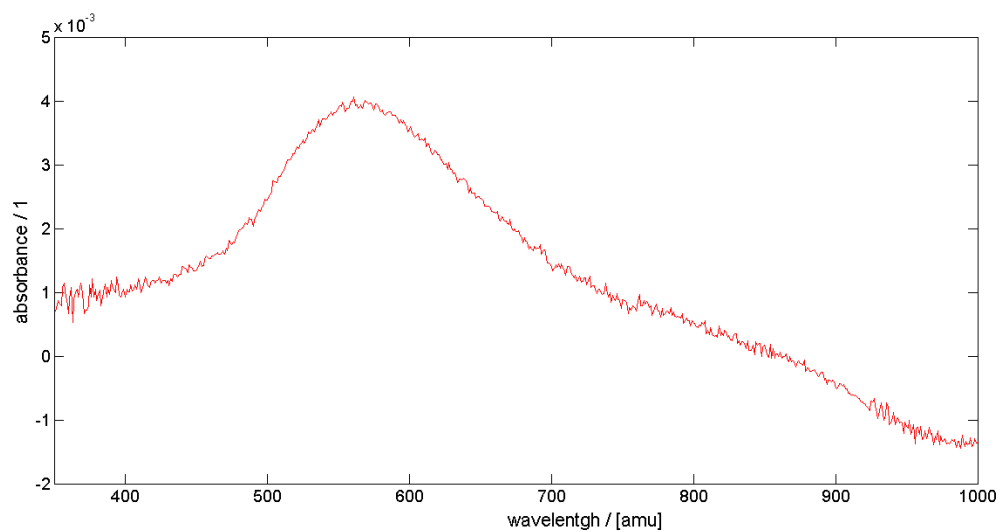


Figure 7.2: Absorption spectrum of gold cluster deposited onto a fused silica plate. Here the absorption peak for Au is between 500 nm and 700 nm.

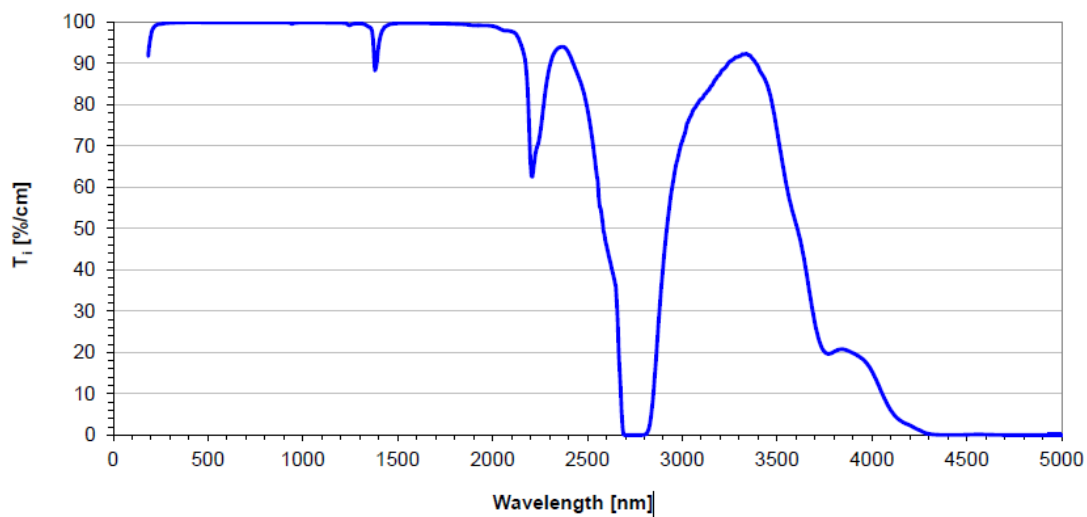


Figure 7.3: Transmittance of the used fused quartz. Taken from⁵⁴

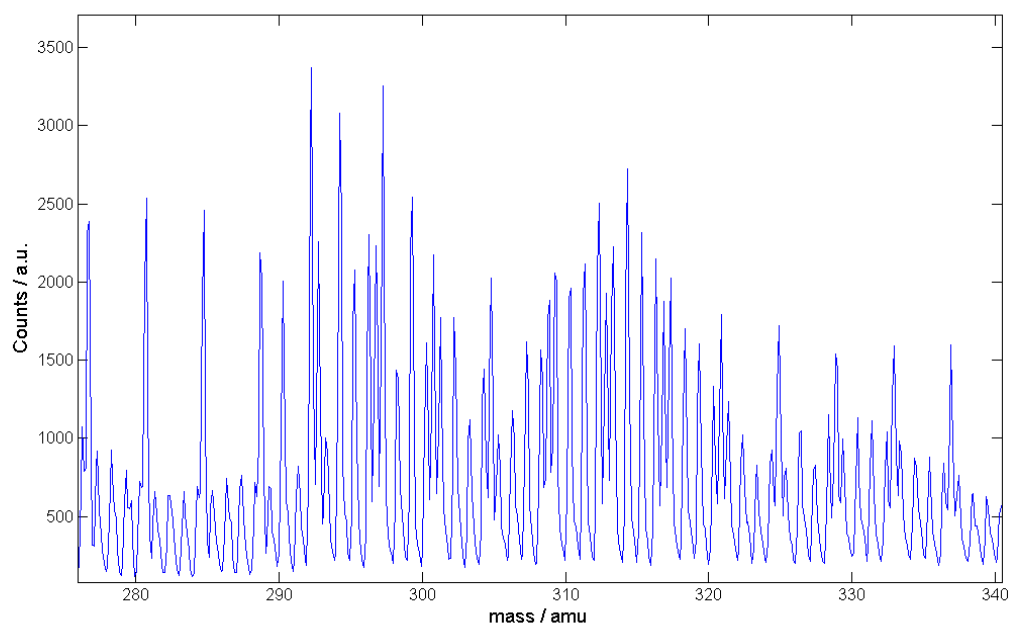
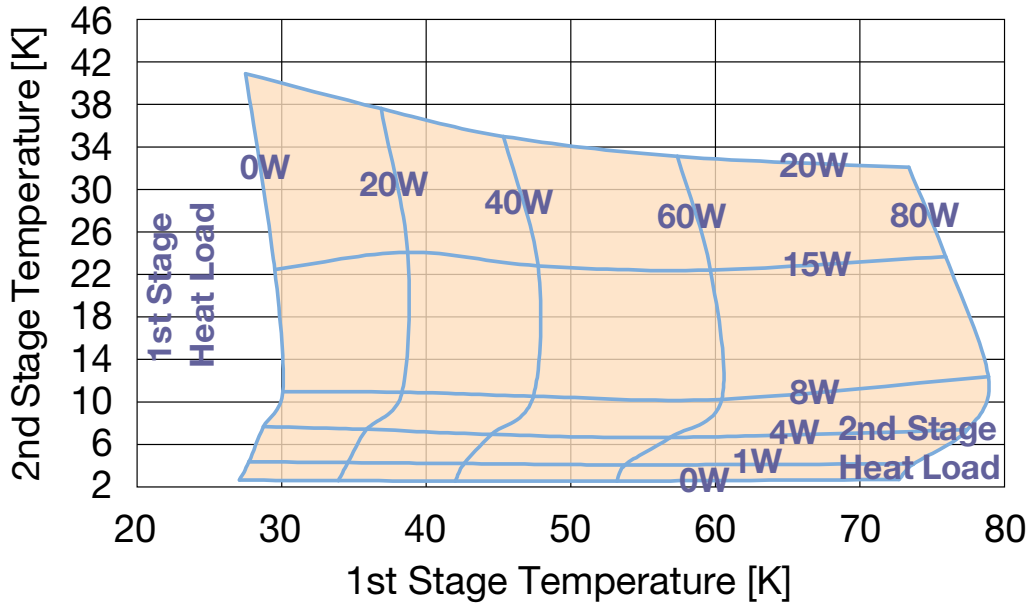


Figure 7.4: Mixed Ni and Cu Time of Flight mass spectrum for a six atom cluster.

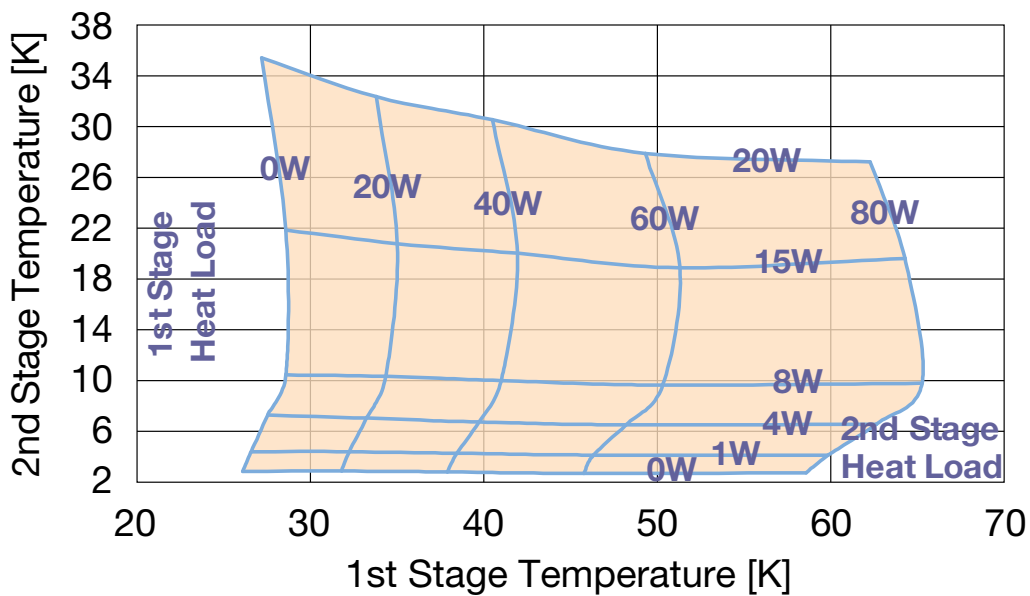


Cryogenics Group

RDK-408D2 Cold Head Capacity Map (50 Hz)



RDK-408D2 Cold Head Capacity Map (60 Hz)



8 Danksagung

An dieser Stelle möchte ich die Möglichkeit nutzen um mich bei allen Personen zu bedanken die mich beim Erstellen dieser Arbeit unterstützt haben.

Meinem Betreuer Prof. Wolfgang Ernst danke ich dafür, die Möglichkeit bekommen zu haben, diese Arbeit zu schreiben. Trotz seines mehr als vollen Terminkalenders kam die Betreuung niemals zu kurz.

Meinen Kollegen Roman Messner, Alexander Schiffmann und Florian Lackner möchte ich für die tolle Zusammenarbeit und das einzigartig gute Arbeitsklima danken, meinen nun schon seit knapp vierzehn Jahren langen Freund Martin Schnedlitz, mit dem ich nun seit der ersten Klasse des Gymnasiums zusammen für Prüfungen gelernt habe und die ganze Zeit des Studiums hindurch, auch: Danke für deine oftmals gut gemeinten Ratschläge auch wenn ich ein Sturkopf sein kann.

Daniel Knez der immer ein offenes Ohr für Anliegen hatte wenn es um Versuche ging und mit dem ich eine sehr lustige Messtage verbringen konnte. Mein ganzes Studium wären nicht möglich gewesen hätte nicht mein Vater Ingo mich so unterstützt und gefördert. Ich kann gar nicht genug dafür danken, dass du mich so unterstützt hast obwohl du meinen Bruder und mich alleine großgezogen hast. Danke auch an meinen Bruder, der der beste Bruder ist den ich mir wünschen kann.

9 Bibliography

- [1] J. Zhu, "Surface plasmon resonance from bimetallic interface in Au–Ag core–shell structure nanowires," *Nanoscale Research Letters*, vol. 4, no. 9, p. 977, 2009.
- [2] B. N. Wanjala, J. Luo, R. Loukrakpam, B. Fang, D. Mott, P. N. Njoki, M. Engelhard, H. R. Naslund, J. K. Wu, L. Wang, *et al.*, "Nanoscale alloying, phase-segregation, and core-shell evolution of gold-platinum nanoparticles and their electrocatalytic effect on oxygen reduction reaction," *Chemistry of Materials*, vol. 22, no. 14, pp. 4282–4294, 2010.
- [3] P. Strasser, S. Koh, T. Anniyev, J. Greeley, K. More, C. Yu, Z. Liu, S. Kaya, D. Nordlund, H. Ogasawara, *et al.*, "Lattice-strain control of the activity in dealloyed core–shell fuel cell catalysts," *Nature Chemistry*, vol. 2, no. 6, pp. 454–460, 2010.
- [4] Y.-Y. Luk, M. Kato, and M. Mrksich, "Self-assembled monolayers of alkanethiolates presenting mannitol groups are inert to protein adsorption and cell attachment," *Langmuir*, vol. 16, no. 24, pp. 9604–9608, 2000.
- [5] J. Gao, H. Gu, and B. Xu, "Multifunctional magnetic nanoparticles: design, synthesis, and biomedical applications," *Accounts of chemical research*, vol. 42, no. 8, pp. 1097–1107, 2009.
- [6] C. Sun, J. S. Lee, and M. Zhang, "Magnetic nanoparticles in MR imaging and drug delivery," *Advanced Drug Delivery Reviews*, vol. 60, no. 11, pp. 1252–1265, 2008.
- [7] S. Eustis and M. A. El-Sayed, "Why gold nanoparticles are more precious than pretty gold: noble metal surface plasmon resonance and its enhancement of the radiative and nonradiative properties of nanocrystals of different shapes," *Chemical Society Reviews*, vol. 35, no. 3, pp. 209–217, 2006.
- [8] P. K. Jain, X. Huang, I. H. El-Sayed, and M. A. El-Sayed, "Noble metals on the nanoscale: optical and photothermal properties and some applications in imaging, sensing, biology, and medicine," *Accounts of Chemical Research*, vol. 41, no. 12, pp. 1578–1586, 2008.
- [9] K. Yu. Arutyunov, "Negative magnetoresistance of ultra-narrow superconducting nanowires in the resistive state," *Physica C*, vol. 468, pp. 272–275, 2008.

-
- [10] M. Dreher, F. Pauly, J. Heurich, J. C. Cuevas, E. Scheer, and P. Nielaba, "Structure and conductance histogram of atomic-sized Au contacts," *Phys. Rev. B*, vol. 72, p. 075435, 2005.
- [11] G. Zhu, S. Zhang, Z. Xu, J. Ma, and X. Shen, "Ultrathin ZnS single crystal nanowires: Controlled synthesis and room-temperature ferromagnetism properties," *J. Am. Chem. Soc.*, vol. 133, pp. 15605–15612, 2011.
- [12] H. She, Y. Chen, X. Chen, K. Zhang, Z. Wang, and D.-L. Peng, "Structure, optical and magnetic properties of Ni@ Au and Au@ Ni nanoparticles synthesized via non-aqueous approaches," *Journal of Materials Chemistry*, vol. 22, no. 6, pp. 2757–2765, 2012.
- [13] M. Heinebrodt, N. Malinowski, F. Tast, W. Branz, I. Billas, and T. Martin, "Bonding character of bimetallic clusters $Au_n X_m$ ($x = Al, In, Cs$)," *The Journal of chemical physics*, vol. 110, no. 20, pp. 9915–9921, 1999.
- [14] M. Gaudry, E. Cottancin, M. Pellarin, J. Lermé, L. Arnaud, J. Huntzinger, J. Vialle, M. Broyer, J. Rousset, M. Treilleux, *et al.*, "Size and composition dependence in the optical properties of mixed (transition metal/noble metal) embedded clusters," *Physical Review B*, vol. 67, no. 15, p. 155409, 2003.
- [15] C.-C. Kim, C. Wang, Y.-C. Yang, Y. Hwu, S.-K. Seol, Y.-B. Kwon, C.-H. Chen, H.-W. Liou, H.-M. Lin, G. Margaritondo, *et al.*, "X-ray synthesis of nickel–gold composite nanoparticles," *Materials Chemistry and Physics*, vol. 100, no. 2, pp. 292–295, 2006.
- [16] A. L. Koh, K. Bao, I. Khan, W. E. Smith, G. Kothleitner, P. Nordlander, S. A. Maier, and D. W. McComb, "Electron energy-loss spectroscopy (EELS) of surface plasmons in single silver nanoparticles and dimers: influence of beam damage and mapping of dark modes," *ACS Nano*, vol. 3, no. 10, pp. 3015–3022, 2009.
- [17] J. P. Toennies and A. F. Vilesov, "Superfluid helium droplets: a uniquely cold nanomatrix for molecules and molecular complexes," *Angew. Chem. Int. Ed.*, vol. 43, no. 20, pp. 2622–2648, 2004.
- [18] H. Buchenau, E. L. Knuth, J. Northby, J. P. Toennies, and C. Winkler, "Mass spectra and time-of-flight distributions of helium cluster beams," *J. Chem. Phys.*, vol. 92, pp. 6875–6889, 1990.
- [19] U. Henne and J. P. Toennies, "Electron capture by large helium droplets," *J. Chem. Phys.*, vol. 108, pp. 9327–9338, 1998.

- [20] L. F. Gomez, E. Loginov, R. Sliter, and A. F. Vilesov, "Sizes of large He droplets," *J. Chem. Phys.*, vol. 135, p. 154201, 2011.
- [21] M. Lewerenz, B. Schilling, and J. Toennies, "A new scattering deflection method for determining and selecting the sizes of large liquid clusters of ^4He ," *Chemical Physics Letters*, vol. 206, no. 1-4, pp. 381–387, 1993.
- [22] M. Lewerenz, B. Schilling, and J. P. Toennies, "Successive capture and coagulation of atoms and molecules to small clusters in large liquid helium clusters," *J. Chem. Phys.*, vol. 102, pp. 8191–8207, 1995.
- [23] C. Kittel, *Introduction to Solid State Physics*. Hoboken: John Wiley & Sons, 2005.
- [24] D. M. Brink and S. Stringari, "Density of states and evaporation rate of helium clusters," *Z. Phys. D: Atoms, Molecules and Clusters*, vol. 15, no. 3, pp. 257–263, 1990.
- [25] F. Lackner, G. Krois, M. Koch, and W. E. Ernst, "Rubidium on helium droplets: Analysis of an exotic Rydberg complex for $n^* < 20$ and $0 \leq l \leq 3$," *The Journal of Physical Chemistry Letters*, vol. 3, no. 10, pp. 1404–1408, 2012.
- [26] K. K. Lehmann and A. M. Dokter, "Evaporative cooling of helium nanodroplets with angular momentum conservation," *Physical review letters*, vol. 92, no. 17, p. 173401, 2004.
- [27] F. Ancilotto, M. Pi, and M. Barranco, "Vortex arrays in nanoscopic superfluid helium droplets," *Phys. Rev. B*, vol. 91, p. 100503(R), 2015.
- [28] L. F. Gomez, K. R. Ferguson, J. P. Cryan, C. Bacellar, R. M. P. Tanyag, C. Jones, S. Schorb, D. Anielski, A. Belkacem, C. Bernando, R. Boll, J. Bozek, S. Carron, G. Chen, T. Delmas, L. Englert, S. W. Epp, B. Erk, L. Foucar, R. Hartmann, A. Hexemer, M. Huth, J. Kwok, S. R. Leone, J. H. S. Ma, F. R. N. C. Maia, E. Malmerberg, S. Marchesini, D. M. Neumark, B. Poon, J. Prell, D. Rolles, B. Rudek, A. Rudenko, M. Seifrid, K. R. Siefermann, F. P. Sturm, M. Swiggers, J. Ullrich, F. Weise, P. Zwart, C. Bostedt, O. Gessner, and A. F. Vilesov, "Shapes and vorticities of superfluid helium nanodroplets," *Science*, vol. 345, pp. 906–909, 2014.
- [29] R. J. Donnelly, *Quantized Vortices in Helium II*. Cambridge: Cambridge University Press, 1991.
- [30] A. M. Ellis and S. Yang, "Model for the charge-transfer probability in helium nanodroplets following electron-impact ionization," *Physical Review A*, vol. 76, no. 3, p. 032714, 2007.

-
- [31] J. Steurer, “Helium droplet mediated fabrication and analysis of noble metal nanoparticles,” Master’s thesis, Graz University of Technology, 2014.
- [32] F. Penning, “Über ionisation durch metastabile atome,” *Naturwissenschaften*, vol. 15, no. 40, pp. 818–818, 1927.
- [33] M. Hartmann, R. E. Miller, *et al.*, “High-resolution molecular spectroscopy of van der Waals clusters in liquid helium droplets,” *Science*, vol. 272, no. 5268, p. 1631, 1996.
- [34] F. Baletto, C. Mottet, and R. Ferrando, “Microscopic mechanisms of the growth of metastable silver icosahedra,” *Phys. Rev. B*, vol. 63, no. 15, p. 155408, 2001.
- [35] D. Reinhard, B. D. Hall, D. Ugarte, and R. Monot, “Size-independent fcc-to-icosahedral structural transition in unsupported silver clusters: an electron diffraction study of clusters produced by inert-gas aggregation,” *Phys. Rev. B*, vol. 55, no. 12, pp. 7868–7881, 1997.
- [36] A. Volk, P. Thaler, M. Koch, E. Fisslthaler, W. Grogger, and W. E. Ernst, “High resolution electron microscopy of Ag-clusters in crystalline and non-crystalline morphologies grown inside superfluid helium nanodroplets,” *J. Chem. Phys.*, vol. 138, p. 214312, 2013.
- [37] P. Thaler, A. Volk, M. Ratschek, M. Koch, and W. E. Ernst, “Molecular dynamics simulation of the deposition process of cold Ag-clusters under different landing conditions,” *J. Chem. Phys.*, vol. 140, p. 044326, 2014.
- [38] P. Thaler, A. Volk, F. Lackner, J. Steurer, D. Knez, W. Grogger, F. Hofer, and W. E. Ernst, “Formation of bimetallic core-shell nanowires along vortices in superfluid He nanodroplets,” *Phys. Rev. B*, vol. 90, p. 155442, 2014.
- [39] C. Lindsay and R. Miller, “Rotational and vibrational dynamics of ethylene in helium nanodroplets,” *The Journal of Chemical Physics*, vol. 122, no. 10, p. 104306, 2005.
- [40] I. Scheele, A. Conjusteau, C. Callegari, R. Schmied, K. K. Lehmann, and G. Scoles, “Near-infrared spectroscopy of ethylene and ethylene dimer in superfluid helium droplets,” *The Journal of Chemical Physics*, vol. 122, no. 10, p. 104307, 2005.
- [41] W. Raith, “Festkörper, band 6 der reihe bergmann-schaefer: Lehrbuch der experimentalphysik,” *Walther de Gruyter, Berlin-New York*, 1992.
- [42] G. Guisbiers, R. Mendoza-Cruz, L. Baza?n-Díaz, J. J. Vela?zquez-Salazar, R. Mendoza-Perez, J. A. Robledo-Torres, J.-L. Rodriguez-Lopez, J. M. Montejano-Carrizales, R. L. Whetten, and M. Jose?-Yacama?n, “Electrum, the gold–silver alloy,

- from the bulk scale to the nanoscale: synthesis, properties, and segregation rules,” *ACS nano*, vol. 10, no. 1, pp. 188–198, 2015.
- [43] M. Tian, N. Kumar, M. H. Chan, and T. E. Mallouk, “Evidence of local superconductivity in granular Bi nanowires fabricated by electrodeposition,” *Physical Review B*, vol. 78, no. 4, p. 045417, 2008.
- [44] “Phasediagram of Au and Ni.” <http://oregonstate.edu/instruct/me581/Homework/ME581LittleBits.html>. Accessed: 2017-02-22.
- [45] S. Heiles, S. Schäfer, and R. Schäfer, “Mass spectrometry and beam deflection studies of tin–lead nanoalloy clusters,” *Physical Chemistry Chemical Physics*, vol. 12, no. 1, pp. 247–253, 2010.
- [46] M. Schnedlitz, “A study of thermally induced surface diffusion processes of monometallicnanowires,” Master’s thesis, Graz University of Technology, 2017.
- [47] W. M. Haynes, *CRC handbook of chemistry and physics*. CRC press, 2014.
- [48] G. Sauerbrey, “Verwendung von Schwingquarzen zur Wägung dünner Schichten und zur Mikrowägung,” *Zeitschrift für physik*, vol. 155, no. 2, pp. 206–222, 1959.
- [49] *Operation Manual Q-pod Quartz Crystal Monitor IPN 074-547-P1B*.
- [50] J. L. Wiza, “Microchannel plate detectors,” *Nuclear Instruments and Methods*, vol. 162, no. 1-3, pp. 587–601, 1979.
- [51] D. B. Williams and C. B. Carter, “The transmission electron microscope,” in *Transmission electron microscopy*, pp. 3–17, Springer, 1996.
- [52] “Wildfire denssolution describtion.” <http://www.denssolutions.com/products/heating/nano-chip/>. Accessed: 2017-05-11.
- [53] *INSTRUCTION MANUAL Operation Guide UV-1800 SHIMADZU SPECTROPHOTOMETER*.
- [54] *Corning® HPFS® 7979, 7980, 8655 Fused Silica Optical Materials Product Information Specialty Materials Division*.
- [55] P. Jaque and A. Toro-Labbé, “Characterization of copper clusters through the use of density functional theory reactivity descriptors,” *The Journal of chemical physics*, vol. 117, no. 7, pp. 3208–3218, 2002.
- [56] W. A. De Heer, “The physics of simple metal clusters: experimental aspects and simple models,” *Reviews of Modern Physics*, vol. 65, no. 3, p. 611, 1993.

- [57] M. Brack, "The physics of simple metal clusters: self-consistent jellium model and semiclassical approaches," *Reviews of modern physics*, vol. 65, no. 3, p. 677, 1993.
- [58] F. Calvo, *Nanoalloys: from fundamentals to emergent applications*. Newnes, 2013.
- [59] I. Katakuse, T. Ichihara, Y. Fujita, T. Matsuo, T. Sakurai, and H. Matsuda, "Mass distributions of copper, silver and gold clusters and electronic shell structure," *International journal of mass spectrometry and ion processes*, vol. 67, no. 2, pp. 229–236, 1985.
- [60] B. Reddy, S. Nayak, S. Khanna, B. Rao, and P. Jena, "Physics of nickel clusters. 2. electronic structure and magnetic properties," *The Journal of Physical Chemistry A*, vol. 102, no. 10, pp. 1748–1759, 1998.
- [61] S. Han, X. Xue, X. Nie, H. Zhai, F. Wang, Q. Sun, Y. Jia, S. Li, and Z. Guo, "First-principles calculations on the role of Ni-doping in Cu_n clusters: From geometric and electronic structures to chemical activities towards CO_2 ," *Physics letters A*, vol. 374, no. 42, pp. 4324–4330, 2010.
- [62] P. A. Derosa, J. M. Seminario, and P. B. Balbuena, "Properties of small bimetallic ni- cu clusters," *The Journal of Physical Chemistry A*, vol. 105, no. 33, pp. 7917–7925, 2001.
- [63] W. Qi, "Size effect on melting temperature of nanosolids," *Physica B: Condensed Matter*, vol. 368, no. 1, pp. 46–50, 2005.
- [64] H. S. Shin, J. Yu, and J. Y. Song, "Size-dependent thermal instability and melting behavior of Sn nanowires," *Applied Physics Letters*, vol. 91, no. 17, p. 173106, 2007.
- [65] S. Zhou, H. Yin, V. Schwartz, Z. Wu, D. Mullins, B. Eichhorn, S. H. Overbury, and S. Dai, "In situ phase separation of NiAu alloy nanoparticles for preparing highly active Au/NiO CO oxidation catalysts," *ChemPhysChem*, vol. 9, no. 17, pp. 2475–2479, 2008.
- [66] D. Knez, P. Thaler, A. Volk, G. Kothleitner, W. E. Ernst, and F. Hofer, "Transformation dynamics of Ni clusters into NiO rings under electron beam irradiation," *Ultramicroscopy*, 2016.
- [67] V. P. Zhdanov and B. Kasemo, "Cabreramott kinetics of oxidation of nm-sized metal particles," *Chemical Physics Letters*, vol. 452, no. 4, pp. 285–288, 2008.
- [68] M. Sakurai, K. Watanabe, K. Sumiyama, and K. Suzuki, "Magic numbers in transition metal (Fe, Ti, Zr, Nb, and Ta) clusters observed by time-of-flight mass spectrometry," *The Journal of Chemical Physics*, vol. 111, no. 1, pp. 235–238, 1999.

-
- [69] M. Schnedlitz, M. Lasserus, D. Knez, A. W. Hauser, F. Hofer, and W. E. Ernst, “Thermally induced breakup of metallic nanowires: Experiment and theory,” *Physical Chemistry Chemical Physics*, 2017.
- [70] L. Jones, “Quantitative adf stem: acquisition, analysis and interpretation,” in *IOP Conference Series: Materials Science and Engineering*, vol. 109, p. 012008, IOP Publishing, 2016.
- [71] J. M. LeBeau, S. D. Findlay, L. J. Allen, and S. Stemmer, “Standardless atom counting in scanning transmission electron microscopy,” *Nano Letters*, vol. 10, no. 11, pp. 4405–4408, 2010.
- [72] T. Fließbach and H. Walliser, *Arbeitsbuch zur Theoretischen Physik: Repetitorium und Übungsbuch*. Springer-Verlag, 2011.
- [73] S. Zhu, T. Chen, Y. Liu, S. Yu, and Y. Liu, “Tunable surface plasmon resonance of gold nanoparticles self-assembled on fused silica substrate,” *Electrochemical and Solid-State Letters*, vol. 13, no. 12, pp. K96–K99, 2010.
- [74] S. Link and M. A. El-Sayed, “Spectral properties and relaxation dynamics of surface plasmon electronic oscillations in gold and silver nanodots and nanorods,” 1999.
- [75] L. J. Sherry, S.-H. Chang, G. C. Schatz, R. P. Van Duyne, B. J. Wiley, and Y. Xia, “Localized surface plasmon resonance spectroscopy of single silver nanocubes,” *Nano Letters*, vol. 5, no. 10, pp. 2034–2038, 2005.